Available online at www.sciencedirect.com
ScienceDirect
Comput. Methods Appl. Mech. Engrg. 397 (2022) 115049
Computer methods in applied mechanics and engineering
www.elsevier.com/locate/cma

A NURBS-based inverse analysis of swelling induced morphing of thin stimuli-responsive polymer gels

N. Vu-Bac[b,f], T. Rabczuk[a,c], H.S. Park[d], X. Fu[e], X. Zhuang[a,b,f,*]

[a] College of Civil Engineering, Tongji University, 1239 Siping Road, 200092 Shanghai, China
[b] Institute of Photonics, Leibniz Universität Hannover, Appelstr. 11A, 30167 Hannover, Germany
[c] Institute of Structural Mechanics, Bauhaus-Universität Weimar, Marienstr. 15, D-99423 Weimar, Germany
[d] Department of Mechanical Engineering, Boston University, Boston, MA 02215, USA
[e] Xi'an Modern Chemistry Research Institute, Xi'an 710065, China
[f] Cluster of Excellence, PHOENIXD, Leibniz Universität Hannover, Germany

Received 4 December 2021; received in revised form 10 April 2022; accepted 23 April 2022
Available online xxxx

Abstract

Gels are a mixture of cross-linked polymers and solvents, and have been widely studied in recent years for a diverse range of biomedical applications. Because gels can undergo large, reversible shape changes due to swelling, their complex physical response must be modeled by coupling large reversible deformation and mass transport. An ongoing challenge in this field is the ability to capture swelling or residual swelling-induced of such stimuli-responsive gels from initially flat two-dimensional (2D) to three-dimensional (3D) curved shapes. Specifically, because such shape changes typically involve large deformations, shape changes, and the exploitation of elastic instabilities, it remains an open question as to what external stimulus should be prescribed to generate a specific target shape. Therefore, we propose a novel formulation that tackles, using both nonlinear kinematics and material models, the coupling between elasticity and solvent transport using Kirchhoff–Love shell theory discretized using isogeometric analysis (IGA). Second, we propose an inverse methodology that chemomechanically couples large deformation and mass transport to identify the external stimuli prescribed to generate a specific target shape. Our numerical examples demonstrate the capability of identifying the required external stimuli, with the implication that the reconstructed target shapes are accurate, including cases where the shape changes due to swelling involve elastic instabilities or softening. Overall, our study can be used to effectively predict and control the large morphological changes of an important class of stimuli-responsive materials.

Keywords: Inverse analysis; Isogeometric analysis; Kirchhoff–Love shells; Stimuli-responsive polymer gels; Instability shape changes

1. Introduction

Elastomeric materials have recently been used extensively in a wide range of biomedical applications. This is because the skeletal network of the elastomeric materials enable them to absorb a large amount of fluid without failure. Instead, elastomers exhibit significant volumetric swelling resulting from insertion of fluid molecules into a

* Corresponding author at: Institute of Photonics, Leibniz Universität Hannover, Appelstr. 11A, 30167 Hannover, Germany.
E-mail address: zhuang@iop.uni-hannover.de (X. Zhuang).

https://doi.org/10.1016/j.cma.2022.115049
0045-7825/

polymer network to form so-called elastomeric gels. Elastomeric gels can be found in food processing, drug delivery and employed in biomedical applications valves for microfluidic devices and tissue engineering. Furthermore, several body parts in humans and animals are likely constituted from the gel materials, see [1].

The interest in elastomeric gels has led to many studies to investigate their behavior. Experimentally, indentation and compression tests which are combined with a modified Biot linear poroelastic theory have been performed to account for the mechanical and transport properties of the materials, see [2–5]. In addition, swelling kinetics have been used to examine material and transport properties of gels. For instance, measuring tip displacement of a swollen cantilever beam including a substrate and a gel, and monitoring planar deformation fields of a swelling gel using fluorescence imaging technique as reported by [6–10].

Furthermore, theoretical and numerical simulations of the elastomeric gels have also been performed to elucidate their behavior in response to external stimuli. These simulations are non-trivial, with challenges in both modeling the large deformation of membranes, as well as their stimuli-responsiveness, as shape changes of soft structures induced by multiple non-mechanical stimuli [11] involve additional complexities. Since an elastomeric gel can be considered as a model system where solvent transport and elasticity are coupled, diffusion of the fluid through the network and resultant deformation of the polymer system should be simulated to account for the behavior of the responsive materials accurately. Tanaka et al. [12] presented kinetics of the materials in an early study. Since then, the response of gels, i.e. the swelling, drying and squeezing phenomena of fluid, due to mechanical stimuli or forced permeation has been studied through coupled diffusion–deformation models, see [11] for instance. Nonlinear modeling of the materials where the fluid–solid mixture is assumed as a homogeneous medium so that a mass flux of the fluid can be considered has been studied, see [1,13–15].

Gels are fabricated in the membrane forms which can particularly [16,17] be transformed into three-dimensional (3D) curved shapes, e.g in self-shaping materials. Upon small variation of environmental conditions, wettability and adhesion of different species in the gels can be changed. Chemical and biochemical signals can also be converted into optical, electrical, thermal and mechanical signals, and vice versa. Therefore, these materials become more important in several applications such as tissue engineering, ‘smart’ optical system and bisensors, microelectromechanical systems. It is known that there are two distinct processes, i.e. concurrent deformation and solvent transport, involved in gels [18]. For instance, when subjected to an external stimuli (e.g. temperature change, change in the concentration of an enzyme) a drug loaded in a gel can migrate out [18]. For instance, when subjected to an external stimuli (e.g. temperature change, change in the concentration of an enzyme) a drug loaded in a gel can migrate out [19]. Elastic instabilities in gels have also been a widely studied topic as reported in [18,20,21], i.e. patterns of crease are observed on the surface [22,23] together with several other forms of buckling [12,24–26]. The shape changes occur as a result of the coupling between in-plane solvent transport and out-of-plane bending. Furthermore, transport properties of solvent on surface differ from those in bulk material [27] that affect spreading and absorption of liquids on surfaces. Another important application of NURBS to soft hyperelastic active media is shown by Nitti et al. [28]. It reported that an electrophysiologic stimulus propagating over a thin cardiac tissue is simulated using Kirchhoff–Love shell theory. However, this interplay between in-plane solvent transport and surface deformations in the context of thin shell structures has not been studied. In order to model the coupling between in-plane solvent transport and surface deformations so that swelling material surfaces can be described accurately, suitable numerical methods are requested.

Several computational models have been developed to study the shape changes, such as buckling of swelling responsive gels in response to external stimuli. The deformation mechanisms of thin shells undergone mechanical stimuli was studied by Non-Euclidean shell theory, see [29]. Kirchhoff–Love shell theory is widely used for modeling thin shell structures as reported in [30,31]. Although avoiding rotational degrees of freedom leads to the lower computational expense, C^1 continuous discretizations are required within the finite element (FE) method of the Kirchhoff–Love shells. NURBS-based FE discretizations are thus employed to fulfill the C^1-continuity requirement of the Kirchhoff–Love shell theory as well as plate theory [32–36]. To the best of our knowledge, this study presents the first formulation used to tackle, using both nonlinear kinematics and material models, the coupling between elasticity and solvent transport using Kirchhoff–Love shell theory.

Furthermore, although shape changes and the associated behavior of the soft materials in response to various prescribed stimuli have been studied, see [37–39], little work upon determining the external stimuli needed to generate the desired shapes from which the morphological changes can be controlled. Therefore, an inverse analysis paradigm is proposed in this study, which also couples nonlinear kinematics and material response, to identify the external stimuli and reconstruct a specific target shape where instability/elastic softening shape changes are allowed.

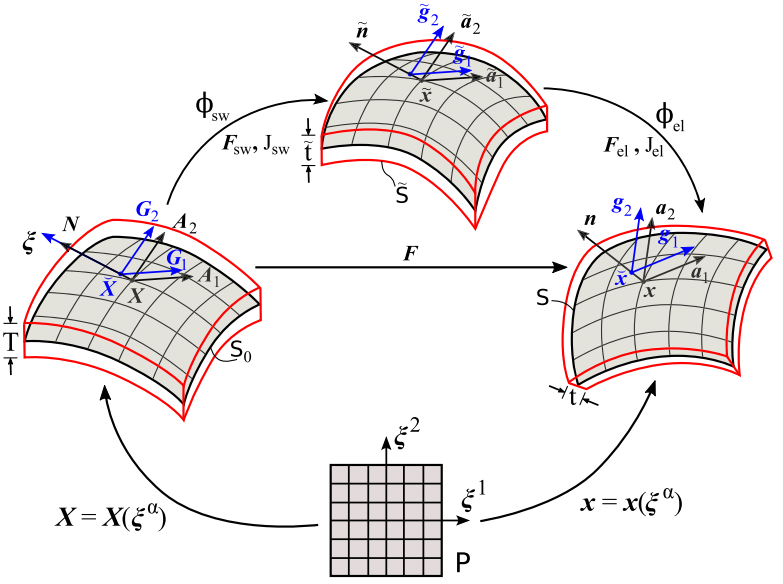

Fig. 1. Mapping from the parameter domain to the reference and spatial configurations. Schematic description for multiplicative decomposition $\boldsymbol{F} = \boldsymbol{F}_{\text{el}}\ \boldsymbol{F}_{\text{sw}}$. The covariant basis vectors and the corresponding normal vectors denoted by $\{\boldsymbol{G}_\alpha, \boldsymbol{N}\}$ for the reference, $\{\tilde{\boldsymbol{g}}_\alpha, \tilde{\boldsymbol{n}}\}$ for the intermediate and $\{\boldsymbol{g}_\alpha, \boldsymbol{n}\}$ for the spatial configurations are shown respectively.

In what follows, we review the thin shell kinematics and the multiplicative decomposition which is an essential kinematical ingredient. In the next section, we briefly present the local force balance and the balance law for fluid content. The free energy based on the Flory–Huggins theory [40,41] characterizing mixing of the fluid with the polymer network is discussed subsequently. The constitutive equations for the free energy, elastic stress, and chemical potential are then summarized. In Section 9, numerical examples are examined to demonstrate the performance of the proposed model. Finally, we close with concluding remarks in Section 10.

Notations

In this study, both index notation and absolute notation are used to express vectors and tensors. Generally, scalars are printed italics, bold face italic letters indicate vectors and tensors, while the discretized quantities at the element level are printed as bold face letters. Latin indices take values 1, 2, 3 and Greek indices take values 1, 2. Quantities associated with the reference and current configurations are denoted by uppercase and lowercase letters, respectively. Standard characters indicate operators. General equations are expressed in terms of the compact matrix notation, while index notation is used to show detailed derivations. The operators "$\cdot$" refers the scalar product, "$\times$" denotes the vector product and the tensor product (or dyadic product) is denoted by "$\otimes$". Furthermore, Einstein's summation convention is also applied.

The scalar product and tensor product of two vectors $\boldsymbol{a}$ and $\boldsymbol{b}$ are given by

$$\boldsymbol{a} \cdot \boldsymbol{b} = a_i\ b_i,$$
$$(\boldsymbol{a} \otimes \boldsymbol{b})_{ij} = a_i\ b_j.$$

Let denote $\boldsymbol{A}$ and $\boldsymbol{B}$ as second-order tensors, then

$$(\boldsymbol{A} \cdot \boldsymbol{B})_{ij} = A_{ik}\ B_{kj}.$$

2. Thin shell kinematics

Considering a general fluid-free homogeneous surface, the spatial coordinates $\boldsymbol{x}$ can be described by the following mapping (see Fig. 1)

$$\boldsymbol{x} = \boldsymbol{x}(\boldsymbol{\xi}^\alpha), \tag{1}$$

with $\boldsymbol{\xi}^{\alpha} = (\xi^1, \xi^2)$ denoting coordinates in the parameter domain $\mathcal{P}$. Let introduce the kinematical referential quantities $\boldsymbol{x}$, $\boldsymbol{a}_{\alpha}$, $\boldsymbol{a}^{\alpha}$, $a_{\alpha\beta}$, and $b_{\alpha\beta}$ are associated with $\mathcal{S}$, and $\boldsymbol{X}$, $\boldsymbol{A}_{\alpha}$, $\boldsymbol{A}^{\alpha}$, $A_{\alpha\beta}$, and $B_{\alpha\beta}$ are the spatial ones associated with $\mathcal{S}_0$. The respective covariant basis vectors $\boldsymbol{a}_{\alpha}$ and $\boldsymbol{A}_{\alpha}$ are given by

$$\begin{aligned} \boldsymbol{a}_{\alpha} &= \frac{\boldsymbol{x}}{\boldsymbol{\xi}^{\alpha}}, \\ \boldsymbol{A}_{\alpha} &= \frac{\boldsymbol{X}}{\boldsymbol{\xi}^{\alpha}} \end{aligned} \tag{2}$$

On the midsurfaces $\mathcal{S}$ and $\mathcal{S}_0$, the unitary normal vectors are expressed respectively as

$$\begin{aligned} \boldsymbol{n} &= \frac{\boldsymbol{a}_1 \times \boldsymbol{a}_2}{\| \boldsymbol{a}_1 \times \boldsymbol{a}_2 \|}, \\ \boldsymbol{N} &= \frac{\boldsymbol{A}_1 \times \boldsymbol{A}_2}{\| \boldsymbol{A}_1 \times \boldsymbol{A}_2 \|}, \end{aligned} \tag{3}$$

and the respective covariant metric coefficients are provided by

$$\begin{aligned} a_{\alpha\beta} &= \boldsymbol{a}_{\alpha} \cdot \boldsymbol{a}_{\beta}, \\ A_{\alpha\beta} &= \boldsymbol{A}_{\alpha} \cdot \boldsymbol{A}_{\beta}. \end{aligned} \tag{4}$$

The corresponding tensors of contravariant metric represented by $[A^{\alpha\beta}] = [A_{\alpha\beta}]^{-1}$ and $[a^{\alpha\beta}] = [a_{\alpha\beta}]^{-1}$ are then determined. The contravariant bases are given by $\boldsymbol{A}^{\alpha} = A^{\alpha\beta}\boldsymbol{A}_{\beta}$ and $\boldsymbol{a}^{\alpha} = a^{\alpha\beta}\boldsymbol{a}_{\beta}$. The curvature coefficients yield

$$\begin{aligned} B_{\alpha\beta} &= \boldsymbol{N} \cdot \boldsymbol{A}_{\alpha,\beta}, \\ b_{\alpha\beta} &= \boldsymbol{n} \cdot \boldsymbol{a}_{\alpha,\beta}. \end{aligned} \tag{5}$$

That leads to the mean, Gaussian curvatures of the deformed configuration $\mathcal{S}$ under the following forms

$$H = \frac{1}{2} a^{\alpha\beta} b_{\alpha\beta}, \quad \kappa = \frac{\det[b_{\alpha\beta}]}{\det[a_{\alpha\beta}]}, \quad \kappa_{1/2} = H \pm \sqrt{H^2 - \kappa}. \tag{6}$$

and the principal curvatures of $\mathcal{S}$ as follows

$$\kappa_{1/2} = H \pm \sqrt{H^2 - \kappa}. \tag{7}$$

Given the mapping in Eq. (1), the respective surface gradient and the surface divergence denoted by $\nabla_{\mathrm{s}}(\bullet)$ and $\nabla_{\mathrm{s}} \cdot (\bullet)$ follow as

$$\begin{aligned} \nabla_{\mathrm{s}} \mu &\coloneqq \mu_{;\alpha}\, \boldsymbol{a}^{\alpha}, \\ \nabla_{\mathrm{s}} \cdot \boldsymbol{v} = \mathrm{div}_{\mathrm{s}} \boldsymbol{v} &\coloneqq \boldsymbol{v}_{;\alpha} \cdot \boldsymbol{a}^{\alpha}, \end{aligned} \tag{8}$$

where μ and $\boldsymbol{v}$ denote general scalars and vectors with $v^{\alpha} \coloneqq \boldsymbol{v} \cdot \boldsymbol{a}^{\alpha}$. Note that for general scalar and vector, the covariant derivative and the parametric one of μ and $\boldsymbol{v}$ coincide, i.e. $\mu_{;\alpha} = \mu_{,\alpha}$ and $\boldsymbol{v}_{;\alpha} = \boldsymbol{v}_{,\alpha}$, see [42]. Other kinematical quantities such as the mean H, Gaussian κ and principal $\kappa_{1/2}$ curvatures can be found in [30]. The surface deformation gradient characterizing the mapping $\boldsymbol{X} \to \boldsymbol{x} = \boldsymbol{\varphi}(\boldsymbol{X})$ reads

$$\boldsymbol{F} \coloneqq \boldsymbol{a}_{\alpha} \otimes \boldsymbol{A}^{\alpha}. \tag{9}$$

The right surface Cauchy–Green tensor results from the surface deformation gradient $\boldsymbol{F}$

$$\boldsymbol{C} \coloneqq \boldsymbol{F}^{\mathrm{T}} \cdot \boldsymbol{F} = a_{\alpha\beta}\ \boldsymbol{A}^{\alpha} \otimes \boldsymbol{A}^{\beta}. \tag{10}$$

Introducing

$$\begin{aligned} \varepsilon_{\alpha\beta} &\coloneqq \frac{1}{2}\left(a_{\alpha\beta} - A_{\alpha\beta}\right), \\ \kappa_{\alpha\beta} &\coloneqq b_{\alpha\beta} - B_{\alpha\beta}, \end{aligned} \tag{11}$$

the Green Lagrange strain and the curvature tensors at a material point on the mid-surface, see [43,44], are then defined by

$$\begin{aligned} \boldsymbol{E} &= \varepsilon_{\alpha\beta}\ \boldsymbol{A}^{\alpha} \otimes \boldsymbol{A}^{\beta}, \\ \boldsymbol{K} &= \kappa_{\alpha\beta} \boldsymbol{A}^{\alpha} \otimes \boldsymbol{A}^{\beta}. \end{aligned} \tag{12}$$

2.1. Variation of kinematical quantities

In order to address the formulations in the subsequent sections, the variation of various kinematic variables are introduced here. Let us consider an kinematical variation in the direction of $\boldsymbol{x}$, denoted by $\delta\boldsymbol{x}$, we have then the variations $\delta\boldsymbol{a}_\alpha = \delta\boldsymbol{x}_{,\alpha}$ and $\delta\boldsymbol{a}_{\alpha,\beta} = \delta\boldsymbol{x}_{,\alpha\beta}$. The variation of the covariant components from Eqs. ((4).1) and ((5).1) follows

$$\begin{aligned} \delta a_{\alpha\beta} &= \boldsymbol{a}_\alpha \cdot \delta\boldsymbol{a}_\beta + \delta\boldsymbol{a}_\alpha \cdot \boldsymbol{a}_\beta, \\ \delta b_{\alpha\beta} &= \boldsymbol{a}_{\alpha,\beta} \cdot \delta\boldsymbol{n} + \boldsymbol{n} \cdot \delta\boldsymbol{a}_{\alpha,\beta} \end{aligned} \tag{13}$$

with

$$\delta\boldsymbol{n} = -(\boldsymbol{a}^\alpha \otimes \boldsymbol{n})\ \delta\boldsymbol{a}_\alpha. \tag{14}$$

Further variation of other kinematical quantities can be found in [45].

2.2. Kinematics of the multiplicative decomposition split

The theory is based on the multiplicative decomposition of the total surface deformation gradient shown by [46]

$$\boldsymbol{F} = \boldsymbol{F}_{\mathrm{el}} \cdot \boldsymbol{F}_{\mathrm{sw}}. \tag{15}$$

$\boldsymbol{F}_{\mathrm{sw}}$ and $\boldsymbol{F}_{\mathrm{el}}$ denote the respective swelling and elastic deformation gradients with the swelling being considered as isotropic

$$\begin{aligned} \boldsymbol{F}_{\mathrm{el}} &= \boldsymbol{a}_\alpha \otimes \tilde{\boldsymbol{a}}^\alpha \\ \boldsymbol{F}_{\mathrm{sw}} &= \tilde{\boldsymbol{a}}_\alpha \otimes \boldsymbol{A}^\alpha. \end{aligned} \tag{16}$$

At the intermediate configuration, the covariant and contravariant bases yield

$$\begin{aligned} \tilde{\boldsymbol{a}}_\alpha &= \boldsymbol{F}_{\mathrm{el}}^{-1}\ \boldsymbol{a}_\alpha, \\ \tilde{\boldsymbol{a}}^\alpha &= \boldsymbol{F}_{\mathrm{el}}^{\mathrm{T}}\ \boldsymbol{a}^\alpha. \end{aligned} \tag{17}$$

Generally, the decomposition shown by Eq. (15) is not unique due to an arbitrary rigid-body rotation imposed upon $\tilde{\mathcal{S}}$ in the stress-free state [47]. However, the uniqueness of the decomposition can be enforced by additional constraint of the material model employed. For instance, the intermediate configuration $\tilde{\mathcal{S}}$ can be defined uniquely, if swelling occurs without rotation. Once isotropic swelling is assumed, the surface swelling deformation gradient is characterized by a scalar λ_{sw} and the referential surface identity tensor $\boldsymbol{I}$, that follows

$$\boldsymbol{F}_{\mathrm{sw}} = \lambda_{\mathrm{sw}}\ \boldsymbol{I}, \quad \lambda_{\mathrm{sw}} > 0 \tag{18}$$

where $\boldsymbol{I} = \boldsymbol{A}_\alpha \otimes \boldsymbol{A}^\alpha$ is the referential surface identity tensor. Here, we assume that long polymer chains and small molecules subjected to large deformation are individually incompressible as stated by [13]. The gel is considered as condensed matter, i.e. voids existing in the gel are neglected, the molecular incompressibility constraint is then enforced by

$$1 + \Omega\ c_R = \det{}_{\mathrm{s}}\boldsymbol{F}_{\mathrm{sw}} = J_{\mathrm{sw}}, \tag{19}$$

with c_R representing the *fluid content* which is defined as the number of fluid molecules absorbed by the polymer per unit volume of the reference configuration at dry state, and Ω being the volume of a mole of fluid molecules, see [1]. The swelling surface stretch λ_{sw} is thus given by

$$\lambda_{\mathrm{sw}} = (1 + \Omega\ c_R)^{1/2}. \tag{20}$$

The right surface Cauchy–Green deformation tensor $\boldsymbol{C}$ is pushed forward to the intermediate configuration using Eq. (17)

$$\boldsymbol{C}_{\mathrm{el}} = \boldsymbol{F}_{\mathrm{el}}^{\mathrm{T}} \cdot \boldsymbol{F}_{\mathrm{el}} = a_{\alpha\beta}\ \tilde{\boldsymbol{a}}^\alpha \otimes \tilde{\boldsymbol{a}}^\beta. \tag{21}$$

Likewise the left surface Cauchy–Green tensor $\boldsymbol{B}$ is pulled back to the intermediate configuration, that is

$$\boldsymbol{B}_{\mathrm{sw}} \coloneqq \boldsymbol{F}_{\mathrm{el}}^{-1} \cdot \boldsymbol{B} \cdot \boldsymbol{F}_{\mathrm{el}}^{-\mathrm{T}} \tag{22}$$

The area change due to the swelling deformation is determined by Eq. (19) and the covariant and contravariant basis vectors associated with $\tilde{\mathrm{S}}$ read

$$\tilde{\boldsymbol{a}}_\alpha = \lambda_{\mathrm{sw}}\, \boldsymbol{A}_\alpha, \quad \tilde{\boldsymbol{a}}^\alpha = \lambda_{\mathrm{sw}}^{-1}\, \boldsymbol{A}^\alpha, \tag{23}$$

The elastic surface deformation gradient $\boldsymbol{F}_{\mathrm{el}}$ and the corresponding surface change J_{el} are obtained from Eq. (15)

$$\boldsymbol{F}_{\mathrm{el}} = \boldsymbol{F} \cdot \boldsymbol{F}_{\mathrm{sw}}^{-1} = \boldsymbol{a}_\alpha \otimes \tilde{\boldsymbol{a}}^\alpha. \tag{24}$$

Note that the elastic surface deformation gradient $\boldsymbol{F}_{\mathrm{el}}$ will be employed in the elastic free-energy computation. If we introduce the strain tensor associated with the intermediate configuration,

$$\tilde{\boldsymbol{e}} \coloneqq \varepsilon_{\alpha\beta} \tilde{\boldsymbol{a}}^\alpha \otimes \tilde{\boldsymbol{a}}^\beta. \tag{25}$$

This strain results from the pull-back of the surface Euler strain $\boldsymbol{e}$, i.e.

$$\tilde{\boldsymbol{e}} \coloneqq \boldsymbol{F}_{\mathrm{sw}}^T\ \boldsymbol{E}\ \boldsymbol{F}_{\mathrm{sw}}^{-1} = \boldsymbol{F}_{\mathrm{el}}^T\ \boldsymbol{e}\ \boldsymbol{F}_{\mathrm{el}}. \tag{26}$$

Noticing that $\boldsymbol{E} \coloneqq \frac{1}{2}(\boldsymbol{C} - \boldsymbol{I})$ and $\boldsymbol{e} \coloneqq \frac{1}{2}\left(\boldsymbol{i} - \boldsymbol{B}^{-1}\right)$ with $\boldsymbol{i} = \boldsymbol{a}_\alpha \otimes \boldsymbol{a}^\alpha$ denoting the spatial surface identity tensor, we obtain

$$\tilde{\boldsymbol{e}} \coloneqq \frac{1}{2}\ \left(\boldsymbol{C}_{\mathrm{el}} - \boldsymbol{B}_{\mathrm{sw}}^{-1}\right). \tag{27}$$

We then define

$$\begin{aligned} \tilde{\boldsymbol{e}}_{\mathrm{el}} &\coloneqq \frac{1}{2}\ \left(\boldsymbol{C}_{\mathrm{el}} - \tilde{\boldsymbol{i}}\right) \\ \tilde{\boldsymbol{e}}_{\mathrm{sw}} &\coloneqq \frac{1}{2}\ \left(\tilde{\boldsymbol{i}} - \boldsymbol{B}_{\mathrm{sw}}^{-1}\right). \end{aligned} \tag{28}$$

with $\tilde{\boldsymbol{i}} = \tilde{\boldsymbol{a}}_\alpha \otimes \tilde{\boldsymbol{a}}^\alpha$ being the intermediate surface identity tensor. The surface Green–Lagrange strain tensor in Eq. (26) can be written in terms of an additive decomposition as

$$\tilde{\boldsymbol{e}} = \tilde{\boldsymbol{e}}_{\mathrm{el}} + \tilde{\boldsymbol{e}}_{\mathrm{sw}}. \tag{29}$$

The decomposition of the components thus can be expressed as

$$\varepsilon_{\alpha\beta} = \varepsilon_{\alpha\beta}^{\mathrm{el}} + \varepsilon_{\alpha\beta}^{\mathrm{sw}} \tag{30}$$

with

$$\begin{aligned} \varepsilon_{\alpha\beta}^{\mathrm{el}} &\coloneqq \frac{1}{2}\left(a_{\alpha\beta} - \tilde{a}_{\alpha\beta}\right), \\ \varepsilon_{\alpha\beta}^{\mathrm{sw}} &\coloneqq \frac{1}{2}\left(\tilde{a}_{\alpha\beta} - A_{\alpha\beta}\right) \end{aligned} \tag{31}$$

Similarly, we can write

$$\kappa_{\alpha\beta} = \kappa_{\alpha\beta}^{\mathrm{el}} + \kappa_{\alpha\beta}^{\mathrm{sw}} \tag{32}$$

with

$$\begin{aligned} \kappa_{\alpha\beta}^{\mathrm{el}} &\coloneqq b_{\alpha\beta} - \tilde{b}_{\alpha\beta} \\ \kappa_{\alpha\beta}^{\mathrm{sw}} &\coloneqq \tilde{b}_{\alpha\beta} - B_{\alpha\beta}, \end{aligned} \tag{33}$$

The decomposition shown in Eq. (15) leads to

$$J = J_{\mathrm{el}}\ J_{\mathrm{sw}} \tag{34}$$

in which

$$\begin{aligned} J_{\mathrm{el}} &= \det{}_{\mathrm{s}} \boldsymbol{F}_{\mathrm{el}} = \sqrt{\frac{\det[a_{\alpha\beta}]}{\det[\tilde{a}_{\alpha\beta}]}}, \\ J_{\mathrm{sw}} &= \det{}_{\mathrm{s}} \boldsymbol{F}_{\mathrm{sw}} = \sqrt{\frac{\det[\tilde{a}_{\alpha\beta}]}{\det[A_{\alpha\beta}]}}. \end{aligned} \tag{35}$$

Remark. In the case of isotropic swelling, an infinitesimal unit cube expands uniformly in all directions. In contrast, the unit cube changes to a rectangular prism shape for anisotropic swelling. While the anisotropic swelling case is clearly more complex than the isotropic one, in case of swelling-induced deformations in bilayer thin plates or in fiber-reinforced materials where expansion takes place in a privileged direction, anisotropic models have to be taken into account.

3. Balance laws

The coupled governing partial differential equations (PDEs) including the local force balance for the Cauchy stress and the local balance for the fluid concentration will be presented briefly in this section.

3.1. Balance of momentum

The equilibrium equation of the thin shell at a spatial point $\boldsymbol{x} \in \mathcal{S}$ in the presence of a body force $\boldsymbol{f}$ is given by [44] as follows

$$\rho\ \dot{\boldsymbol{v}} = \boldsymbol{T}^{\alpha}_{;\alpha} + \boldsymbol{f}, \tag{36}$$

where ρ is the total density and $\boldsymbol{v} := \dot{\boldsymbol{x}}$ is the material velocity at $\boldsymbol{x}$; $\boldsymbol{T}^{\alpha}_{;\alpha}$ represents the covariant derivative of $\boldsymbol{T}^{\alpha}$. The internal traction $\boldsymbol{T}^{\alpha}$ exerting upon the cross-sectional plane normal to $\boldsymbol{a}^{\alpha}$ is expressed by

$$\boldsymbol{T}^{\alpha} = \boldsymbol{\sigma}^{\mathrm{T}}\ \boldsymbol{a}^{\alpha} = N^{\alpha\beta}\ \boldsymbol{a}_{\beta} + S^{\alpha}\ \boldsymbol{n}. \tag{37}$$

Here we define the surface Cauchy stress tensor

$$\boldsymbol{\sigma} = N^{\alpha\beta}\ \boldsymbol{a}_{\alpha} \otimes \boldsymbol{a}_{\beta} + S^{\alpha}\ \boldsymbol{a}_{\alpha} \otimes \boldsymbol{n}, \tag{38}$$

where the in-plane membrane and the out-of-plane shear components of the sectional force are shown respectively by

$$\begin{aligned} N^{\alpha\beta} &= \sigma^{\alpha\beta} + b^{\alpha}_{\gamma}\ M^{\gamma\beta}, \\ S^{\alpha} &= -M^{\beta\alpha}_{;\beta}. \end{aligned} \tag{39}$$

We introduce the stress in the configuration $\tilde{\mathcal{S}}$ using the pull-back formula

$$\tilde{\boldsymbol{\sigma}} := J_{\mathrm{el}}\ \tilde{\boldsymbol{F}}^{-1}_{\mathrm{el}}\ \boldsymbol{\sigma}\ \tilde{\boldsymbol{F}}^{-\mathrm{T}}_{\mathrm{el}}, \tag{40}$$

and insert Eq. (38) into Eq. (40) that leads to

$$\tilde{\boldsymbol{\sigma}} := \tilde{N}^{\alpha\beta}\ \tilde{\boldsymbol{a}}_{\alpha\beta} \otimes \tilde{\boldsymbol{a}}_{\beta} + \tilde{S}^{\alpha}\ \tilde{\boldsymbol{a}}_{\alpha} \otimes \tilde{\boldsymbol{n}} \tag{41}$$

where $\tilde{\boldsymbol{F}}_{\mathrm{el}} := \boldsymbol{F}_{\mathrm{el}} + \boldsymbol{n} \otimes \boldsymbol{N}$. Likewise, the bending moment tensor[1]

$$\boldsymbol{\mu} = -M^{\alpha\beta}\ \boldsymbol{a}_{\alpha} \otimes \boldsymbol{a}_{\beta}. \tag{42}$$

In the same manner as $\boldsymbol{\sigma}$, $\boldsymbol{\mu}$ can be pulled back from $\mathcal{S}$ to $\tilde{\mathcal{S}}$

$$\tilde{\boldsymbol{\mu}} = J_{\mathrm{el}}\ \tilde{\boldsymbol{F}}^{-1}_{\mathrm{el}}\ \boldsymbol{\mu}\ \tilde{\boldsymbol{F}}^{-\mathrm{T}}_{\mathrm{el}} = -\tilde{M}^{\alpha\beta}\ \tilde{\boldsymbol{a}}_{\alpha} \otimes \tilde{\boldsymbol{a}}_{\beta} \tag{43}$$

in which $\tilde{M}^{\alpha\beta} := J_{\mathrm{el}}\ M^{\alpha\beta}$.

3.2. Balance law for the fluid concentration

The governing equation for the fluid content on surface is shown by [48] as

$$\frac{\partial c_R}{\partial t} = -J\ j^{\alpha}_{;\alpha} \tag{44}$$

[1] Non-italic moment $\boldsymbol{\mu}$ should not be confused with italic chemical potential field μ and nodal chemical potential $\boldsymbol{\mu}_e$.

where $j^{\alpha}_{;\alpha}$ is the covariant derivative of $j^{\alpha} = \boldsymbol{j} \cdot \boldsymbol{a}^{\alpha}$, with $\boldsymbol{j}$ being spatial surface fluid flux. The fluid flux is related to the spatial surface chemical potential gradient $\nabla\mu$ by a "Darcy-type" law as

$$j^{\alpha} = -m\ a^{\alpha\beta}\ \mu_{;\beta}, \tag{45}$$

with m being a mobility coefficient for an isotropic material. Introducing the polymer volume fraction defined by

$$\phi := \frac{1}{1 + \Omega\ c_R} = \lambda_{\mathrm{sw}}^{-2}, \quad 0 < \phi \leq 1, \tag{46}$$

Note that $\phi = 1$ represents the dry state, and $\phi < 1$ shows a swollen state. We can then rewrite the above equation as follows

$$\frac{\dot{\phi}}{J\ \Omega\ \phi^2} - j^{\alpha}_{;\alpha} = 0. \tag{47}$$

As mentioned above, we have the important swelling constraint (kinematical constraint) between c_R and J_{sw} shown by Eq. (19). Here, we consider a permeable shell in which a pure solvent (a small molecule) and a solution (a long polymer chain) are separated so that the solvent can diffuse through the membrane until the solution exerts the so-called osmotic pressure, that follows

$$\mu = \frac{\partial \psi}{\partial c_R} + p\ \Omega \tag{48}$$

The osmotic pressure can be interpreted by the Lagrange multiplier, see [1]. The pressure enhances the chemical potential that results in movement of the fluid solvent into the gel. The chemical potential is given by [48]

$$\mu = \mu^0 + k_B\vartheta \left[\ln(1-\phi) + \phi + \chi\phi^2 - \frac{\Omega K}{k_B\vartheta}\ \ln(J\phi) + \frac{1}{2}\frac{\Omega K}{R\vartheta}\ \ln(J\phi)^2 \right]. \tag{49}$$

where k_B is the Boltzmann's constant, ϑ is the constant temperature, χ denotes Flory–Huggins interaction parameter, and K is the bulk modulus. The Dirichlet and Neumann boundary conditions for the displacement and surface traction read

$$\begin{aligned} \boldsymbol{u} &= \bar{\boldsymbol{u}} \quad \text{on } \partial_u \mathcal{S}, \\ \boldsymbol{t} &= \bar{\boldsymbol{t}} \quad \text{on } \partial_t \mathcal{S}. \end{aligned} \tag{50}$$

Boundary conditions for the chemical potential and the fluid flux read

$$\begin{aligned} \mu &= \bar{\mu} \quad \partial_{\mu}\mathcal{S}, \\ -\boldsymbol{j} \cdot \boldsymbol{\nu} &= \bar{j} \quad \text{on } \partial_j \mathcal{S} \end{aligned} \tag{51}$$

3.3. Balance of surface energy

We consider here a spatial computational domain $\mathcal{R}$ subjected to the external body force $\boldsymbol{f}$ and the surface traction vector $\boldsymbol{T}$ on the boundary $\partial\mathcal{R}$ normal to $\boldsymbol{\nu} = \nu_{\alpha}\ \boldsymbol{a}^{\alpha}$. If we ignore the kinetic energy and assume that inertial effects are negligible, the surface energy balance can be written as

$$\frac{d}{dt}\int_{\mathcal{R}} \psi\ \mathrm{da} = \int_{\mathcal{R}} \boldsymbol{v} \cdot \boldsymbol{f}\ \mathrm{da} + \int_{\partial\mathcal{R}} \boldsymbol{v} \cdot \boldsymbol{T}\ \mathrm{ds} - \int_{\partial\mathcal{R}} \mu\ j_{\nu}\ \mathrm{ds}, \quad \forall \mathcal{R} \subset \mathcal{S}. \tag{52}$$

where $\boldsymbol{v} := \dot{\boldsymbol{x}}$ denote the current surface velocity. The last term in Eq. (52) accounts for the flux of energy entered into $\mathcal{R}$ across $\partial\mathcal{R}$ (i.e. fluid energy of a boundary influx j_{ν}). Introducing the surface fluid flux vector $\boldsymbol{j} = j^{\alpha}\ \boldsymbol{a}_{\alpha}$ through

$$j_{\nu} = -\boldsymbol{j} \cdot \boldsymbol{\nu} = -j^{\alpha}\ \nu_{\alpha}. \tag{53}$$

Then applying the surface divergence theorem to the terms in Eq. (52) and noticing the surface balance laws shown by Eqs. (36) and (44), we have

$$\frac{d}{dt}\int_{\mathcal{R}} \psi\ \mathrm{da} = \int_{\mathcal{R}} \left(\frac{1}{2}\sigma^{\alpha\beta}\ \dot{a}_{\alpha\beta} + M^{\alpha\beta}\ \dot{b}_{\alpha\beta} \right)\ \mathrm{da} + \int_{\mathcal{R}} \left(\mu\ \dot{c_R} - j^{\alpha}\ \mu_{;\alpha} \right)\ \mathrm{da}, \quad \forall \mathcal{R} \subset \mathcal{S}. \tag{54}$$

Making use of the localization theorem upon Eq. (54) leads to

$$\dot{\psi} = \frac{1}{2}\ \sigma^{\alpha\beta}\ \dot{a}_{\alpha\beta} + M^{\alpha\beta}\ \dot{b}_{\alpha\beta} + \mu\ \dot{c_R} - j^{\alpha}\ \mu_{;\alpha}, \quad \forall \boldsymbol{x} \in \mathcal{S}. \tag{55}$$

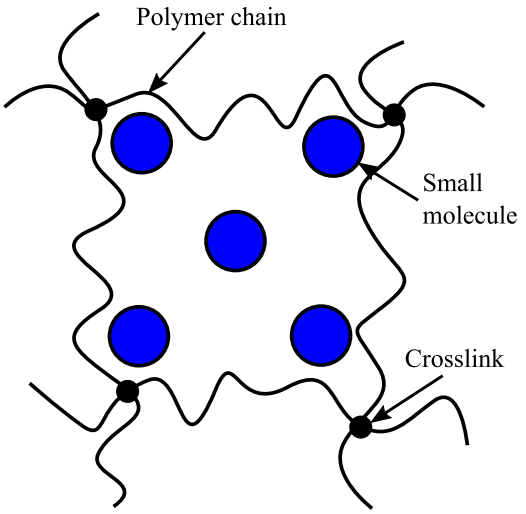

Fig. 2. A schematic of structure of the gel [18].

4. Constitutive equations

Elastomeric materials can absorb a large amount of fluid molecules which aggregate into a gel as shown in Fig. 2. The small molecules within the gel can migrate over a long distance and interact by weak physical bonds, see [18]. We notice that the swelling induced volume change per unit reference volume is characterized by $J_{\text{sw}} - 1 = \Omega\, c_R$. It is assumed that this change results from the change in fluid solvent (small molecules in the gel). The swelling constraint can be then shown by Eq. (19). Within the scope of the thermodynamics of swelling, a free-energy functional form for polymeric gels where the entropy of stretching the polymer network is combined with the entropy of mixing the polymers with the solvent was proposed by Flory et al. [49]. In this way, the coupling between the fields of deformation of the polymer network and the fluid concentration is through the constitutive equations.

4.1. Surface Helmholtz free energy

In this study, we consider a coupled fluid diffusion and large deformation of elastomeric gels. Therefore, the Helmholtz free energy density ψ depends on the elastic strains $\varepsilon^{\text{el}}_{\alpha\beta}$ and $\kappa^{\text{el}}_{\alpha\beta}$ and the fluid concentration c_R.

$$\psi = \psi(\varepsilon^{\text{el}}_{\alpha\beta}, \kappa^{\text{el}}_{\alpha\beta}, c_R). \tag{56}$$

It can be written in additive chemical, mixing and mechanical contributions as follows

$$\psi = \mu^0\, c_R + \psi_{\text{mix}}(c_R) + \psi_{\text{mech}}(\varepsilon^{\text{el}}_{\alpha\beta}, \kappa^{\text{el}}_{\alpha\beta}), \tag{57}$$

where μ^0 is the chemical potential of the fluid, ψ_{mix} is the free energy change resulting from mixing of the fluid with the polymer network, and ψ_{mech} is the free energy change due to the elastic stretching of the polymer network. The surface Cauchy stress, moment and the chemical potential at the deformed configuration take the form

$$\begin{aligned} \sigma^{\alpha\beta} &= \frac{\partial \psi}{\partial \varepsilon^{\text{el}}_{\alpha\beta}}, \\ M^{\alpha\beta} &= \frac{\partial \psi}{\partial \kappa^{\text{el}}_{\alpha\beta}}, \\ \mu &= \frac{\partial \psi}{\partial c} \end{aligned} \tag{58}$$

Introducing the Helmholtz free energy density at the intermediate configuration $\tilde{\psi}$ as proposed by [46], the Cauchy stress and moment can be rewritten as

$$\begin{aligned} \sigma_{\mathrm{el}}^{\alpha\beta} &= \frac{1}{J_{\mathrm{el}}} \frac{\partial \tilde{\psi}}{\partial \varepsilon_{\alpha\beta}^{\mathrm{el}}}, \\ M_{\mathrm{el}}^{\alpha\beta} &= \frac{1}{J_{\mathrm{el}}} \frac{\partial \tilde{\psi}}{\partial \kappa_{\alpha\beta}^{\mathrm{el}}} \end{aligned} \tag{59}$$

If we introduce the referential density by $\rho^0 = J\ \rho$, the total energy can be written as

$$\Psi = \int_{\mathcal{S}_0} \rho^0\ \psi\ \mathrm{dA} \tag{60}$$

Similarly, if we define $\tilde{\rho} = J_{\mathrm{el}}\ \rho$ to be the density associated with $\tilde{\mathcal{S}}$ and notice $\mathrm{d}\tilde{a} = J_{\mathrm{sw}}\ \mathrm{dA}$, the free energy density associated with the intermediate configuration reads

$$\Psi = \int_{\mathcal{S}_0} \tilde{\rho}\ \psi\ \mathrm{d}\tilde{a} \tag{61}$$

in which

$$\Psi = \tilde{\rho}\ \psi \tag{62}$$

The elastic stress and moment components $\sigma^{\alpha\beta}$ and $M^{\alpha\beta}$ can be rewritten in alternative form as follows

$$\begin{aligned} \tilde{\sigma}_{\mathrm{el}}^{\alpha\beta} &= \frac{\partial \tilde{\psi}}{\partial \varepsilon_{\alpha\beta}^{\mathrm{el}}} = \frac{\partial \tilde{\psi}}{\partial \varepsilon_{\alpha\beta}}, \\ \tilde{M}_{\mathrm{el}}^{\alpha\beta} &= \frac{\partial \tilde{\psi}}{\partial \kappa_{\alpha\beta}^{\mathrm{el}}} = \frac{\partial \tilde{\psi}}{\partial \kappa_{\alpha\beta}}, \end{aligned} \tag{63}$$

4.2. Free energy due to mixing

As mentioned above a gel is the mixture of a 3D network of polymer chains and a species of small molecules that forms a liquid solution. The free energy of mixing is adopted from Flory [40]

$$\psi_{\mathrm{mix}} = \frac{k_B\ \vartheta}{\Omega}\ \frac{1}{\phi}\left((1-\phi)\ \ln(1-\phi) + \chi\ \phi\ (1-\phi)\right). \tag{64}$$

In the parenthesis, the entropy of mixing is represented by the first term while the second term represents the enthalpy of mixing [40]. The enthalpy of mixing infers the gel swells, i.e. the fluid molecules to enter the gel, if χ is decreased resulting and vice versa, see [1,40]. The mixing energy can be rewritten as a function c_R as follows

$$\psi_{\mathrm{mix}} = k_B\ \vartheta\ c_R \left(\ln\left(\frac{\Omega\ c_R}{1+\Omega\ c_R}\right) + \chi\left(\frac{1}{1+\Omega\ c_R}\right)\right) \tag{65}$$

4.3. Free energy due to elastic stretching

The constitution using Kirchhoff–Love shell theory is formulated from classical 3D constitutive model as presented by [50]. Hence, the stored surface energy density $\psi = \psi(\varepsilon_{\mathrm{el}}^{\alpha\beta}, \kappa_{\mathrm{el}}^{\alpha,\beta}, c)$ can be derived from the 3D free energy density $\hat{\psi} = \hat{\psi}(\hat{\boldsymbol{C}}_{\mathrm{el}}, c)$ in which $\hat{\boldsymbol{C}}_{\mathrm{el}}$ is the 3D elastic right Cauchy–Green tensor. This is performed by projecting 3D models upon the intermediate surface $\tilde{\mathcal{S}}$. According to Chester et al. [1], most of elastomeric polymers are incompressible materials from mechanical point of view. As standard consideration, the permeating fluid behaves as incompressible. Hence, the elastomeric gels are treated as incompressible homogeneous materials such that the constraint

$$g_{\mathcal{L}} := 1 - \hat{J}_{\mathrm{el}} = 0 \tag{66}$$

is included in the free energy [31]. The free energy takes the functional form of the 3D incompressible Neo-Hookean material model as follows

$$\hat{\psi}_{\text{mech}}(\hat{I}_1^{\text{el}}, \hat{J}_{\text{el}}, p) = \frac{\hat{G}_{\text{shear}}}{2}\left(\hat{I}_1^{\text{el}} - 3\right) + p\left(1 - \hat{J}_{\text{el}}\right) \tag{67}$$

where the invariants $\hat{I}_1^{\text{el}} := \hat{\boldsymbol{C}}_{\text{el}} : \mathbf{1}$ and $\hat{J}_{\text{el}} := \sqrt{\det \hat{\boldsymbol{C}}_{\text{el}}}$ with $\hat{\boldsymbol{C}}_{\text{el}}$ being the 3D elastic Cauchy–Green tensor, $\mathbf{1}$ denoting the identity tensor in $\mathbb{R}^3$, $\hat{G}_{\text{shear}}$ denoting the 3D shear modulus. The Lagrange multiplier p appearing in the last term is used to apply the area-incompressible constraint. Consequently, the 3D Kirchhoff stress components can be stated by

$$\hat{\tau}^{\alpha\beta} = \hat{\tilde{\sigma}}_{\text{el}}^{\alpha\beta} = \hat{G}_{\text{shear}}\left(\tilde{g}^{\alpha\beta} - \frac{1}{J_{\text{el}}^{\star 2}}\, g^{\alpha\beta}\right). \tag{68}$$

where $g^{\alpha\beta}$ and $\tilde{g}^{\alpha\beta}$ are the respective spatial and intermediate contravariant metric components at an arbitrary point (P) in the shell continuum, $J_{\text{el}}^{\star}$ is the invariant of $\boldsymbol{C}^{\star}$ and defined as

$$J_{\text{el}}^{\star} := \sqrt{\det \boldsymbol{C}^{\star}} = \sqrt{\frac{g}{\tilde{g}}} \tag{69}$$

with $\boldsymbol{C}^{\star} = g_{\alpha\beta}\ \tilde{\boldsymbol{g}}^{\alpha} \otimes \tilde{\boldsymbol{g}}^{\beta}$, $g := \det[g_{\alpha\beta}]$ and $\tilde{g} := \det[\tilde{g}_{\alpha\beta}]$. Here, $\tilde{\boldsymbol{g}}^{\alpha}$ denotes the contravariant base vector and $g_{\alpha\beta}$, $\tilde{g}_{\alpha\beta}$ denote the spatial and intermediate covariant metric components at P, respectively.

In this shell theory the 2D material equations with all the involved variables on the midsurface are addressed. However, it is noted that they are derived from the 3D incompressible Neo-Hookean material model. In this way, numerical through-the-thickness integration of the 3D elasticity matrix has to be used to obtain the nonlinear material law. Projecting the 3D Kirchhoff stress $\hat{\tilde{\tau}}^{\alpha\beta}$ on surface and using numerical integration result in the projected elastic Kirchhoff stress and moment

$$\begin{aligned}
\tilde{\tau}^{\alpha\beta} &= \int_{-\frac{T}{2}}^{\frac{T}{2}} \tilde{s}\left(1 - \xi^2\kappa\right)\ \hat{\tilde{\tau}}^{\alpha\beta}\ d\xi, \\
\tilde{M}^{\alpha\beta} &= \int_{-\frac{T}{2}}^{\frac{T}{2}} \tilde{s}\left(-\xi + H\xi^2\right)\ \hat{\tilde{\tau}}^{\alpha\beta}\ d\xi,
\end{aligned} \tag{70}$$

where

$$\tilde{s} = 1 + 2\tilde{H}\xi + \tilde{\kappa}\xi^2. \tag{71}$$

Here, κ and H can be referred in Section 2, T denotes the shell thickness and the coordinate in thickness direction $\xi \in [-T/2\ \ T/2]$. More details of the projection technique and description of the kinematical quantities such as $g_{\alpha\beta}$, $g^{\alpha\beta}$, $\tilde{g}_{\alpha\beta}$, $\tilde{g}^{\alpha\beta}$, and $\tilde{H}$, $\tilde{\kappa}$ can be found in [31,50].

Remark. According to Beatty [51], Neo-Hookean material and Mooney–Rivlin material models are ideally used to describe behavior of soft materials. The Neo-Hookean material, which is a particular kind of Mooney–Rivlin material, was established based on the statistical mechanics of the amorphous structure of rubberlike materials. The Neo-Hookean model has been widely used to describe the incompressible hyperelastic material model in modeling the morphological changes of soft materials, e.g. [1,37,52]. The Neo-Hookean material model, Eq. (67) is chosen due to its convexity that ensures stable characteristic in large deformation. In particular, the second derivative of the free energy with respect to (w.r.t.) the strain, i.e. the material tangent tensor, is positive definite. As such, the Neo-Hookean model is widely used to represent the nearly incompressible, large deformation behavior of soft materials.

5. Weak forms

5.1. Mechanical model

Multiplying the strong form Eq. (36) with the admissible variation $\delta\boldsymbol{x}$ and taking integration upon the domain $\mathcal{S}$ result in the weak form of the mechanical model

$$G_{\text{int}} - G_{\text{ext}} = 0 \quad \forall \delta\boldsymbol{x} \in \mathcal{U}_0, \tag{72}$$

with $\delta \boldsymbol{x}$ selected to be zero on the Dirichlet boundary, but non-zero on the surface, i.e. $\mathcal{U}_0 = \{\delta \boldsymbol{x} \in \mathcal{H}^2(\mathcal{S}(\boldsymbol{x})) \mid \delta \boldsymbol{x} = 0 \text{ on } \partial_x \mathcal{S}\}$, where $\mathcal{H}^2$ is C^1 continuous. The internal and external virtual works can be expressed as

$$\begin{aligned} G_{\text{int}} &= \int_{\mathcal{S}} \frac{1}{2} \delta a_{\alpha\beta}\ \sigma^{\alpha\beta}\ \text{da} + \int_{\mathcal{S}} \delta b_{\alpha\beta}\ M^{\alpha\beta}\ \text{da}, \\ G_{\text{ext}} &= \int_{\mathcal{S}} \delta \boldsymbol{x} \cdot \boldsymbol{f}\ \text{da} + \int_{\partial_t \mathcal{S}} \delta \boldsymbol{x} \cdot \boldsymbol{t}\ \text{ds}. \end{aligned} \tag{73}$$

If noticing $\text{da} = J\ \text{dA} = J_{\text{el}}\ J_{\text{sw}}\ \text{dA}$, the internal virtual work at the reference configuration can be expressed as

$$G_{\text{int}} = \int_{\mathcal{S}_0} \frac{1}{2}\ \delta a_{\alpha\beta}\ \tilde{\tau}^{\alpha\beta}\ J_{\text{sw}}\ \text{dA} + \int_{\mathcal{S}_0} \delta b_{\alpha\beta}\ \tilde{M}^{\alpha\beta}\ J_{\text{sw}}\ \text{dA}. \tag{74}$$

5.2. Fluid content

The weak form of fluid content is obtained by contracting the strong form Eq. (44) with the test function $\delta\mu$ as follows

$$\bar{G}_{\text{in}} + \bar{G}_{\text{int}} - \bar{G}_{\text{ext}} = 0, \quad \forall \delta\mu \in \mathcal{V}_0. \tag{75}$$

Similarly, $\mathcal{V}_0 = \{\delta\mu \in \mathcal{H}^1(\mathcal{S}(\mu, t)) \mid \delta\mu = 0 \text{ on } \partial_\mu \mathcal{S}\}$ where $\mathcal{H}^1$ is C^0 continuous. Multiplying the governing ODE (47) for the fluid concentration with an admissible variation $\delta\mu$ and using the surface divergence theorem yields

$$\int_{\mathcal{S}} \delta\mu\ \frac{\dot{\phi}}{J\ \Omega\ \phi^2}\ \text{da} - \int_{\mathcal{S}} \delta\mu_{;\alpha}\ j^{\alpha}\ \text{da} + \int_{\partial_j \mathcal{S}} \delta\mu\ \boldsymbol{j} \cdot \boldsymbol{v}\ \text{ds} = 0. \tag{76}$$

with

$$\begin{aligned} \bar{G}_{\text{in}} &= \int_{\mathcal{S}} \delta\mu\ \frac{\dot{\phi}}{J\ \Omega\ \phi^2}\ \text{da}, \\ \bar{G}_{\text{int}} &= -\int_{\mathcal{S}} \delta\mu_{;\alpha}\ j^{\alpha}\ \text{da}, \\ \bar{G}_{\text{ext}} &= -\int_{\partial_j \mathcal{S}} \delta\mu\ \boldsymbol{j} \cdot \boldsymbol{v}\ \text{ds}. \end{aligned} \tag{77}$$

Inserting Eq. (45) into Eq. (77).2 and adopting the relations shown in Eq. (8)

$$\bar{G}_{\text{int}} = \int_{\mathcal{S}} m\ \nabla_{\text{s}}(\delta\mu) \cdot\ \nabla_{\text{s}}\mu\ \text{da}. \tag{78}$$

Applying the relationships $\nabla_{\text{s}} \bullet = \boldsymbol{F}^{-\text{T}}\ \nabla_{\text{s0}} \bullet$ and noticing $\text{da} = J\ \text{dA}$ lead to

$$\bar{G}_{\text{int}} = \int_{\mathcal{S}_0} J\ m\ \boldsymbol{C}^{-1}\ \nabla_{\text{s0}}\delta\mu \cdot\ \nabla_{\text{s0}}\mu\ \text{dA}. \tag{79}$$

where $\nabla_{\text{s}}(\bullet)$ and $\nabla_{\text{s0}}(\bullet)$ denote the surface gradient following from Eq. ((8).1) w.r.t. the spatial and material coordinates, respectively.

6. Linearizations

The solution of a coupled diffusion–deformation system is solved by using a Newton–Raphson iteration. It requires the linearizations of the two equilibrium equations (72) and (75). The linearizations of the internal virtual works shown by Eqs. ((73).1) and ((77).2) take the following forms.

$$\begin{aligned} \Delta G_{\text{int}} &= \Delta_x G_{\text{int}} + \Delta_\mu G_{\text{int}}, \\ \Delta \bar{G}_{\text{int}} &= \Delta_x \bar{G}_{\text{int}} + \Delta_\mu \bar{G}_{\text{in}} + \Delta_\mu \bar{G}_{\text{int}}, \end{aligned} \tag{80}$$

where $\Delta_x(\bullet)$ and $\Delta_\mu(\bullet)$ are the respective changes of quantity $(\bullet)$ in the direction of increments $\Delta\boldsymbol{x}$ and $\Delta\mu$. The linearization of G_{int} from Eq. ((80).1) gives

$$\begin{aligned}\Delta G_{\text{int}} = \int_{\mathcal{S}_0} \Big(& \tilde{c}^{\alpha\beta\gamma\delta}\ \frac{1}{2}\delta a_{\alpha\beta}\ \frac{1}{2}\Delta_x a_{\gamma\delta} + \tilde{d}^{\alpha\beta\gamma\delta}\ \frac{1}{2}\delta a_{\alpha\beta}\ \Delta_x b_{\gamma\delta} + \tilde{\tau}^{\alpha\beta}\ \frac{1}{2}\Delta_x \delta a_{\alpha\beta} \\ & + \tilde{e}^{\alpha\beta\gamma\delta}\ \frac{1}{2}\delta b_{\alpha\beta}\ \Delta_x a_{\gamma\delta} + \tilde{f}^{\alpha\beta\gamma\delta}\ \delta b_{\alpha\beta}\ \Delta_x b_{\gamma\delta} + \tilde{M}^{\alpha\beta}\ \Delta_x \delta b_{\alpha\beta} \Big)\ J_{\text{sw}}\ dA \\ & + \int_{\mathcal{S}_0} \left[\left(\frac{1}{2}\delta a_{\alpha\beta}\ \tilde{\tau}^{\alpha\beta} + \delta b_{\alpha\beta}\ \tilde{M}^{\alpha\beta} \right)\ \Delta_\mu J_{\text{sw}} + \left(\frac{1}{2}\delta a_{\alpha\beta}\ \Delta_\mu \tilde{\tau}^{\alpha\beta} + \delta b_{\alpha\beta}\ \Delta_\mu \tilde{M}^{\alpha\beta} \right)\ J_{\text{sw}} \right] \text{dA}.\end{aligned} \tag{81}$$

with

$$\begin{aligned}\tilde{c}^{\alpha\beta\gamma\delta} &:= 2\frac{\partial \tilde{\tau}^{\alpha\beta}}{\partial a_{\gamma\delta}}, \quad \tilde{d}^{\alpha\beta\gamma\delta} := \frac{\partial \tilde{\tau}^{\alpha\beta}}{\partial b_{\gamma\delta}}, \\ \tilde{e}^{\alpha\beta\gamma\delta} &:= 2\frac{\partial \tilde{M}^{\alpha\beta}}{\partial a_{\gamma\delta}}, \quad \tilde{f}^{\alpha\beta\gamma\delta} := \frac{\partial \tilde{M}^{\alpha\beta}}{\partial b_{\gamma\delta}}.\end{aligned} \tag{82}$$

The external mechanical virtual work, Eq. ((73).2), is linearized by

$$\Delta_x G_{\text{ext}} = \int_{\partial\mathcal{S}} m_\tau\ \delta\boldsymbol{a}_\alpha \cdot \left(\nu^\beta \boldsymbol{n} \otimes \boldsymbol{a}^\alpha + \nu^\alpha \boldsymbol{a}^\beta \otimes \boldsymbol{n} \right) \Delta_x \boldsymbol{a}_\beta\ \text{ds}. \tag{83}$$

where m_τ denotes bending moment component acting on $\partial\mathcal{S}$. From Eq. ((80).2) the $\bar{G}_{\text{int}}$ is linearized as follows

$$\begin{aligned}\Delta \bar{G}_{\text{int}} = & \int_{\mathcal{S}_0} m\ \Delta_x J\ \boldsymbol{C}^{-1}\ \nabla_{s0}\delta\mu \cdot \nabla_{s0}\mu\ \text{dA} + \int_{\mathcal{S}_0} J\ m\ \Delta_x \boldsymbol{C}^{-1}\ \nabla_{s0}\delta\mu \cdot \nabla_{s0}\mu\ \text{dA} \\ & + \int_{\mathcal{S}_0} J\ \delta\mu\ \Delta_\mu \left(\frac{\dot{\phi}}{J\ \Omega\ \phi^2} \right)\ \text{dA} - \int_{\mathcal{S}_0} J\ \Delta_\mu m\ \boldsymbol{C}^{-1}\ \nabla_{s0}(\delta\mu) \cdot \nabla_{s0}\mu\ \text{dA} \\ & - \int_{\mathcal{S}_0} J\ m\ \boldsymbol{C}^{-1}\ \nabla_{s0}(\delta\mu) \cdot\ \Delta_\mu\left(\nabla_{s0}\mu\right)\ \text{dA}.\end{aligned} \tag{84}$$

Here, linearizations of the kinematical quantities and their variations such as $\Delta_x J$, $\Delta_x \boldsymbol{C}^{-1}$, $\Delta_x a_{\alpha\beta}$, $\Delta_x b_{\alpha\beta}$, $\Delta_x a^{\alpha\beta}$, $\Delta_x b^{\alpha\beta}$, and $\Delta_x \delta a_{\alpha\beta}$, $\Delta_x \delta b_{\alpha\beta}$ can be found in [31,45]. The linearizations $\Delta_\mu \tilde{\boldsymbol{a}}_\alpha$, $\Delta_\mu \tilde{\boldsymbol{a}}^\alpha$, $\Delta_x \tilde{a}_{\alpha\beta}$, $\tilde{a}^{\alpha\beta}$, $\Delta_\mu \tilde{b}_{\alpha\beta}$, $\Delta_\mu \tilde{b}^{\alpha\beta}$, $\Delta_\mu J_{\text{sw}}$, $\Delta_\mu \tilde{\tau}^{\alpha\beta}$, and $\Delta_\mu \tilde{M}^{\alpha\beta}$, etc. are presented in Appendix.

7. Finite element discretization

7.1. FE approximation

The coupled governing PDEs (72) and (75) are solved by the finite element (FE) method. We consider here sets of elements Ω_0^e, Ω^e and $\tilde{\Omega}^e$ with n_e nodes discretized from the corresponding surface domains $\mathcal{S}_0$, $\mathcal{S}$ and $\tilde{\mathcal{S}}$. Accordingly, $\mathbf{X}_e$, $\mathbf{x}_e$, $\tilde{\mathbf{x}}_e$ and $\boldsymbol{\mu}_e$ are defined as nodal position vectors and chemical potential at FE nodes, respectively. All primary variable fields (i.e geometry and chemical potential) within Ω^{e} and Ω_0^{e} can be then approximated using NURBS interpolation

$$\boldsymbol{X} \approx \mathbf{N}\ \mathbf{X}_e, \quad \boldsymbol{x} \approx \mathbf{N}\ \mathbf{x}_e \quad \text{and} \quad \tilde{\boldsymbol{x}} \approx \mathbf{N}\ \tilde{\mathbf{x}}_e \tag{85}$$

and

$$\mu \approx \bar{\mathbf{N}}\ \boldsymbol{\mu}_e, \tag{86}$$

where $\mathbf{N}(\xi^1, \xi^2) := [\text{N}_1\mathbf{1},\ \text{N}_2\mathbf{1},\ \ldots,\ \text{N}_{n_e}\mathbf{1}]$ is an array shape functions and $\bar{\mathbf{N}}(\xi^1, \xi^2) := [\text{N}_1,\ \text{N}_2, \ldots,\ \text{N}_n]$ is an array shape functions. The discretization of covariant bases follows from Eq. (2) as

$$\boldsymbol{A}_\alpha = \frac{\partial \boldsymbol{X}}{\partial \xi^\alpha} \approx \mathbf{N}_{,\alpha}\ \mathbf{X}_e, \quad \boldsymbol{a}_\alpha = \frac{\partial \boldsymbol{x}}{\partial \xi^\alpha} \approx \mathbf{N}_{,\alpha}\ \mathbf{x}_e \quad \text{and} \quad \tilde{\boldsymbol{a}}_\alpha = \frac{\partial \tilde{\boldsymbol{x}}}{\partial \xi^\alpha} \approx \mathbf{N}_{,\alpha}\ \tilde{\mathbf{x}}_e. \tag{87}$$

The respective variations are discretized in the same fashion

$$\begin{aligned}&\delta\boldsymbol{X} \approx \mathbf{N}\ \delta\mathbf{X}_e, && \delta\boldsymbol{x} \approx \mathbf{N}\ \delta\mathbf{x}_e, && \delta\tilde{\boldsymbol{x}} \approx \mathbf{N}\ \delta\tilde{\mathbf{x}}_e, \\ &\delta\boldsymbol{A}_\alpha \approx \mathbf{N}_{,\alpha}\ \delta\mathbf{X}_e, && \delta\boldsymbol{a}_\alpha \approx \mathbf{N}_{,\alpha}\ \delta\mathbf{x}_e, && \delta\tilde{\boldsymbol{a}}_\alpha \approx \mathbf{N}_{,\alpha}\ \delta\tilde{\mathbf{x}}_e,\end{aligned} \tag{88}$$

and

$$\delta\mu \approx \bar{\mathbf{N}}\ \delta\boldsymbol{\mu}_e. \tag{89}$$

where the derivatives of shape function $\mathbf{N}_{,\alpha} := \partial\mathbf{N}/\partial\xi^\alpha$. The discretized surface gradients of the chemical potential field and its variation then follow

$$\begin{aligned}
&\nabla_{\mathrm{s}}\mu = \mu_{,\alpha}\ \boldsymbol{a}^\alpha \approx \boldsymbol{a}^\alpha\ \bar{\mathbf{N}}_{,\alpha}\ \boldsymbol{\mu}_e, && \nabla_{\tilde{\mathrm{s}}}\mu = \mu_{,\alpha}\ \tilde{\boldsymbol{a}}^\alpha \approx \tilde{\boldsymbol{a}}^\alpha\ \bar{\mathbf{N}}_{,\alpha}\ \boldsymbol{\mu}_e, && \nabla_{\mathrm{s}0}\mu = \mu_{,\alpha}\ \boldsymbol{A}^\alpha \approx \boldsymbol{A}^\alpha\ \bar{\mathbf{N}}_{,\alpha}\ \boldsymbol{\mu}_e,\\
&\nabla_{\mathrm{s}}\delta\mu = \delta\mu_{,\alpha}\ \boldsymbol{a}^\alpha \approx \boldsymbol{a}^\alpha\ \bar{\mathbf{N}}_{,\alpha}\ \delta\boldsymbol{\mu}_e, && \nabla_{\tilde{\mathrm{s}}}\delta\mu = \delta\mu_{,\alpha}\ \tilde{\boldsymbol{a}}^\alpha \approx \tilde{\boldsymbol{a}}^\alpha\ \bar{\mathbf{N}}_{,\alpha}\ \delta\boldsymbol{\mu}_e, && \nabla_{\mathrm{s}0}\delta\mu = \delta\mu_{,\alpha}\ \boldsymbol{A}^\alpha \approx \boldsymbol{A}^\alpha\ \bar{\mathbf{N}}_{,\alpha}\ \delta\boldsymbol{\mu}_e.
\end{aligned} \tag{90}$$

with $\bar{\mathbf{N}}_{,\alpha} := \partial\bar{\mathbf{N}}/\partial\xi^\alpha$ and $\nabla_{\tilde{\mathrm{s}}}(\bullet)$ denotes the surface gradient w.r.t. the coordinate system associated with $\tilde{\mathrm{s}}$. Further crucial kinematic variations can be found in [50].

7.2. Discretized weak forms

The two weak forms for the mechanical and the fluid content components are then discretized using the above approximations. From Eq. (72) it follows that

$$\delta\boldsymbol{x}^{\mathrm{T}}\ [\mathbf{f}_{\mathrm{int}} - \mathbf{f}_{\mathrm{ext}}] = 0 \quad \forall\delta\boldsymbol{x} \in \mathcal{U}_0 \tag{91}$$

and the discretization of Eq. (75) can be written as

$$\delta\boldsymbol{\mu}^{\mathrm{T}}\ \left[\bar{\mathbf{f}}_{\mathrm{in}} + \bar{\mathbf{f}}_{\mathrm{int}} - \bar{\mathbf{f}}_{\mathrm{ext}}\right] = 0 \quad \forall\delta\boldsymbol{\mu} \in \mathcal{V}_0 \tag{92}$$

with

$$\mathbf{f}_{\mathrm{int}} = \sum_{e=1}^{n_{\mathrm{el}}} \mathbf{f}^e_{\mathrm{int}}, \quad \text{and} \quad \mathbf{f}_{\mathrm{ext}} = \sum_{e=1}^{n_{\mathrm{el}}} \mathbf{f}^e_{\mathrm{ext}} \tag{93}$$

and

$$\bar{\mathbf{f}}_{\mathrm{in}} = \sum_{e=1}^{n_{\mathrm{el}}} \bar{\mathbf{f}}^e_{\mathrm{in}}, \quad \bar{\mathbf{f}}_{\mathrm{int}} = \sum_{e=1}^{n_{\mathrm{el}}} \bar{\mathbf{f}}^e_{\mathrm{int}}, \quad \text{and} \quad \bar{\mathbf{f}}_{\mathrm{ext}} = \sum_{e=1}^{n_{\mathrm{el}}} \bar{\mathbf{f}}^e_{\mathrm{ext}}. \tag{94}$$

The mechanical internal force vector at the element level can be expressed as

$$\mathbf{f}^e_{\mathrm{int}} = \underbrace{\int_{\Omega^e_0} \tilde{\tau}^{\alpha\beta}\ \mathbf{N}^T_{,\alpha}\ \boldsymbol{a}_\beta\ J_{\mathrm{sw}}\ \mathrm{dA}}_{\mathbf{f}^e_{\mathrm{int}\tau}} + \underbrace{\int_{\Omega^e_0} \tilde{M}^{\alpha\beta}\ \left(\mathbf{N}_{,\alpha\beta} - \Gamma^\gamma_{\alpha\beta}\ \mathbf{N}_{,\gamma}\right)\ \boldsymbol{n}\ J_{\mathrm{sw}}\ \mathrm{dA}}_{\mathbf{f}^e_{\mathrm{int}M}}, \tag{95}$$

with $\mathbf{f}^e_{\mathrm{int}\tau}$ and $\mathbf{f}^e_{\mathrm{int}M}$ denoting the elastic membrane stress $\tilde{\tau}^{\alpha\beta}$ and bending moment $\tilde{M}^{\alpha\beta}$, respectively, given by

$$\begin{aligned}
\mathbf{f}^e_{\mathrm{int}\tau} &:= \int_{\Omega^e_0} \tilde{\tau}^{\alpha\beta}\ \mathbf{N}^T_{,\alpha}\ \boldsymbol{a}_\beta\ J_{\mathrm{sw}}\ \mathrm{dA},\\
\mathbf{f}^e_{\mathrm{int}M} &:= \int_{\Omega^e_0} \tilde{M}^{\alpha\beta}\ \left(\mathbf{N}_{,\alpha\beta} - \Gamma^\gamma_{\alpha\beta}\ \mathbf{N}_{,\gamma}\right)\ \boldsymbol{n}\ J_{\mathrm{sw}}\ \mathrm{dA},
\end{aligned} \tag{96}$$

where $\mathbf{N}_{,\alpha\beta}(\boldsymbol{\xi}) := [N_{1,\alpha\beta}\mathbf{1}, N_{2,\alpha\beta}\mathbf{1}, \ldots, N_{n,\alpha\beta}\mathbf{1}]$ and $\Gamma^\gamma_{\alpha\beta} = \boldsymbol{a}^\gamma \cdot \boldsymbol{a}_{\alpha,\beta}$. The external force vector is split into three components as follows

$$\begin{aligned}
\mathbf{f}^e_{\mathrm{ext}0} &:= \int_{\Omega^e_0} \mathbf{N}^T\ \boldsymbol{f}_0\ \mathrm{dA},\\
\mathbf{f}^e_{\mathrm{ext}q} &:= \int_{\Omega^e} \mathbf{N}^T\ q\ \boldsymbol{n}\ \mathrm{da},\\
\mathbf{f}^e_{\mathrm{ext}t} &:= \int_{\partial_t\Omega^e} \mathbf{N}^T\ \boldsymbol{t}\ \mathrm{ds}.
\end{aligned} \tag{97}$$

where $\boldsymbol{f}_0$, q and $\boldsymbol{t}$ are the body force, the external pressure prescribed on the surface and the traction, respectively. The discretization of the three force components in Eq. (92) is given by

$$\begin{aligned}
\bar{\mathbf{f}}_{\text{in}} &= \int_{\Omega_0^e} \bar{\mathbf{N}}^{\mathrm{T}} \left(\frac{\dot{\phi}}{\Omega\ \phi^2} \right) \ \mathrm{dA}, \\
\bar{\mathbf{f}}_{\text{int}} &= -\int_{\Omega_0^e} J\ m\ \left[\boldsymbol{A}^{\alpha}\ \bar{\mathbf{N}}_{,\alpha} \right]^{\mathrm{T}}\ \boldsymbol{C}^{-1}\ \left[\boldsymbol{A}^{\alpha}\ \bar{\mathbf{N}}_{,\alpha}\ \boldsymbol{\mu}_e \right]\ \mathrm{dA}, \\
\bar{\mathbf{f}}_{\text{ext}} &= -\int_{\partial_j \Omega^e} \bar{\mathbf{N}}^{\mathrm{T}}\ \boldsymbol{j} \cdot \boldsymbol{v}\ \mathrm{da} = \int_{\partial_j \Omega^e} \bar{\mathbf{N}}^{\mathrm{T}}\ \bar{j}\ \mathrm{ds}.
\end{aligned} \tag{98}$$

8. Inverse analysis

In order to determine the external stimuli, i.e. chemical potential and out-of-plane pressure (or displacement), prescribed to generate a target shape of the soft, thin shells, an inverse analysis is employed. A brief description of an inverse analysis framework for the coupled chemohyperelastic model is summarized in this section. From the mathematical expression, inverse problems can be stated as follows:

$$\begin{aligned}
\text{minimize} \quad & \mathcal{L}\Big(\mathbf{s}, \mathbf{u}(\mathbf{s}), \boldsymbol{\mu}(\mathbf{s})\Big) \\
& h\Big(\mathbf{s}, \mathbf{u}(\mathbf{s}), \boldsymbol{\mu}(\mathbf{s})\Big) = 0 \\
& \mathbf{s}_{\mathrm{l}} \leq \mathbf{s} \leq \mathbf{s}_{\mathrm{u}},
\end{aligned} \tag{99}$$

where $\mathbf{s}$ represents the design variables, while $\mathbf{u}(\mathbf{s})$ and $\boldsymbol{\mu}(\mathbf{s})$ represent the state variables. The inverse solution is solved through a gradient-based optimization technique where the loss function $\mathcal{L}$ subjected to the equality constrains h. The state variable $\mathbf{s}$ is restricted by the lower and the upper bounds $\mathbf{s}_{\mathrm{l}}$, $\mathbf{s}_{\mathrm{u}}$, respectively. Generally, if the measured data at discrete points on the surface are available, the design variables $\mathbf{s}$ can be identified. Making use of the forward operator shown by

$$F : X \rightarrow Y, \tag{100}$$

$$\mathbf{s} \mapsto \{\mathbf{u}, \boldsymbol{\mu}\}^T, \tag{101}$$

a mapping of the design variables to the measured data can be conducted. Here, X denotes a finite dimensional parameter space where the design variables are defined, while Y denotes the one for measurement. Given measurements $\mathbf{u}^{\text{meas}}$ and $\boldsymbol{\mu}^{\text{meas}}$, inverse problem is performed to determine the design variables $\mathbf{s}$, that reads

$$F(\mathbf{s}) = \begin{Bmatrix} \mathbf{u}^{\text{meas}} \\ \boldsymbol{\mu}^{\text{meas}} \end{Bmatrix}. \tag{102}$$

The system of equations (102) may be ill-posed for complex problems. Therefore, we intend to employ a regularized least-squares technique to obtain the solution through an iterative minimization of

$$\mathcal{L}(s, u(s)) = \frac{1}{2} \int_{\Omega} \left| \frac{u^{\text{meas}} - u(s)}{u_{\max}(s)} \right|^2 d\Omega + \frac{1}{2} \int_{\Omega} \left| \frac{\mu^{\text{meas}} - \mu(s)}{\mu_{\max}(s)} \right|^2 d\Omega + R(q) \tag{103}$$

where $u_{\max}$ and $\mu_{\max}$ refer the maximum values of displacement and solvent fields, respectively. $R(q)$ is defined as a regularization term, see [31]. The objective function is discretized by means of finite element (FE), which yields

$$\mathcal{L} = \frac{1}{2} \left\| \frac{\mathbf{u}^{\text{meas}} - \mathbf{u}}{u_{\max}} \right\|^2 + \frac{1}{2} \left\| \frac{\boldsymbol{\mu}^{\text{meas}} - \boldsymbol{\mu}}{\mu_{\max}} \right\|^2 + \boldsymbol{\beta}\ \left\| \boldsymbol{\gamma} - \boldsymbol{\gamma}^0 \right\|^2, \tag{104}$$

with $u_{\max}$ and $\mu_{\max}$ being the respective maximum values of the nodal displacement and chemical potential. The measured values of the displacement and the chemical potential are given by $\mathbf{u}^{\text{meas}}$ and $\boldsymbol{\mu}^{\text{meas}}$, respectively. Here, we take $\boldsymbol{\gamma}^0$ as priori estimates of the external stimuli, while $\boldsymbol{\beta}$ denote the regularization parameters that are determined using the residual L-curve technique as reported by [31]. The moving asymptotes (MMA) method is adopted to obtain the optimal solution in this study. As a gradient-based optimization technique, MMA requires the sensitivity of the objective function $\mathcal{L}$ w.r.t. the design variables $\mathbf{s}$. Here, we use the finite difference method to estimate the

sensitivity, which follows

$$\frac{\mathrm{d}\mathcal{L}}{\mathrm{d}s_i} \approx \frac{\mathcal{L}(\boldsymbol{u}, \boldsymbol{s} + \Delta \boldsymbol{s}_i) - \mathcal{L}(\boldsymbol{u}, \boldsymbol{s})}{\Delta \boldsymbol{s}_i}, \tag{105}$$

where $\mathcal{L}(\boldsymbol{u}, \boldsymbol{s} + \Delta \boldsymbol{s}_i)$ represents a perturbation of the objective function in direction of the variable $\mathbf{s}_i$. According to [53], we select $\Delta \mathbf{s}_i = 0.01 \times \mathbf{s}_i$ so that the truncation error is reduced to acceptable value.

For ill-posed problems which may occur for inverse analysis, Tikhonov regularization is employed together with a residual L-curve criterion. Making use of the L-curve technique, Nanthakumar et al. [54] show a log–log of the residual norm w.r.t. a regularized solution. Hence, a proper regularization parameter whose optimal value can be chosen as an intersection point (knee point) of two flat regions on the curve. It is noted that the two flat regions result from under and over regularization, see [31] for details.

9. Numerical examples

The shape morphing of geometric composite shells induced by the solvent transport is studied in this section. Large deformations on the thin shells induced by swelling of the responsive gels are examined via three numerical examples: (1) free-swelling of a gel; (2) squeezing of an already swollen gel; and (3) swelling of different shell structures driven by fluid concentration gradient. In the representative examples, the nonlinear behavior is represented by the hyperelastic constitution. Lateral pressure (or displacement) is prescribed to trigger out-of-plane deflection. Here we assume the material properties are independent of the temperature. The temperature is also considered uniformly distributed through the thickness. For the sake of convenient discussion hereafter, we denote the shear modulus, the mobility, the diffusion coefficient as G_{shear}, m, and D.

The proposed method is validated using experiment-like data that represent measurements obtained by experiments. The procedure is summarized by the following steps: (1) A NURBS-based FE [55] is implemented to analyze thin shell problems under prescribed external stimuli. The *experiment-like data* are then obtained by $\mathbf{u}^{\text{meas}} = \mathbf{u}^{\text{forw}}\ (1 + 0.01\boldsymbol{\eta})$, with $\boldsymbol{\eta} \in [-0.5, 0.5]$ being randomly generated. The random vector $1 + 0.01\boldsymbol{\eta}$ is used to reflect the noise data affected by different measuring factors; (2) The inverse analysis is employed to reconstruct the shape corresponding to the experiment-like data. This step is conducted using the above-mentioned iterative optimization method. The inverse solution can be obtained once the convergence criterion $err. = \frac{\mathcal{L}^{\mathrm{i}} - \mathcal{L}^{\mathrm{i}-1}}{\mathcal{L}^0} \leq 10^{-3}$ is satisfied. It should be noted that the target configurations are recovered where the shape changes due to instabilities/elastic softening are allowed.

9.1. One-dimensional transient swelling

In order to examine the presented formulations, we consider at first the one-dimensional (1D) transient swelling of responsive gel as shown in Fig. 3.1. A planar sheet with dimensions $L \times H = 2$ cm $\times$ 1 cm is pinned at the bottom $X_1 = 0$ while the top is taken to be traction-free. At the top $X_1 = H$ the polymer sheet is in contact with the solvent. Therefore, the initial condition for the chemical potential of the dry polymer yields

$$\mu(\boldsymbol{X}, t = 0) = \mu_0. \tag{106}$$

At the top the temperature-dependent chemical potential follows

$$\bar{\mu}(t) = \mu^0 + \mu_0\ \exp(-t/t_d), \tag{107}$$

where $\mu^0 = 0$ J denotes the chemical potential of the solvent and $t_d = 300$ s is taken. At the initial dry state $\phi = 0.9999$ is assumed. Fluid flux-free is also prescribed on the top surface. The incompressible Neo-Hookean model is employed for this study. The material properties at room temperature: $G_{\text{shear}} = 0.1$ MPa, $\nu = 0.5$, $\Omega = 1 \times 10^{-4}$ m$^{3/mol}$, $D = 5 \times 10^{-9}$ m$^{2/s}$, $\chi = 0.1$. The computational domain is discretized by 20×10 quadratic NURBS elements.

Figs. 3(b) and 3(c) show plots of the volume fraction ϕ and the inelastic stretch λ_{sw} over the normalized axial coordinate X_1/H_0, respectively. Both quantities show similar behavior with results reported in [1]. The polymer volume fraction ϕ and the inelastic stretch λ_{sw} approach the equilibrium values $\phi_{\text{eq}} \approx 0.3217$ and $\lambda_{\text{eq,sw}} \approx 3.1080$ at the steady state represented by the dashed lines. Furthermore, snapshots of the deformation of the sheet w.r.t.

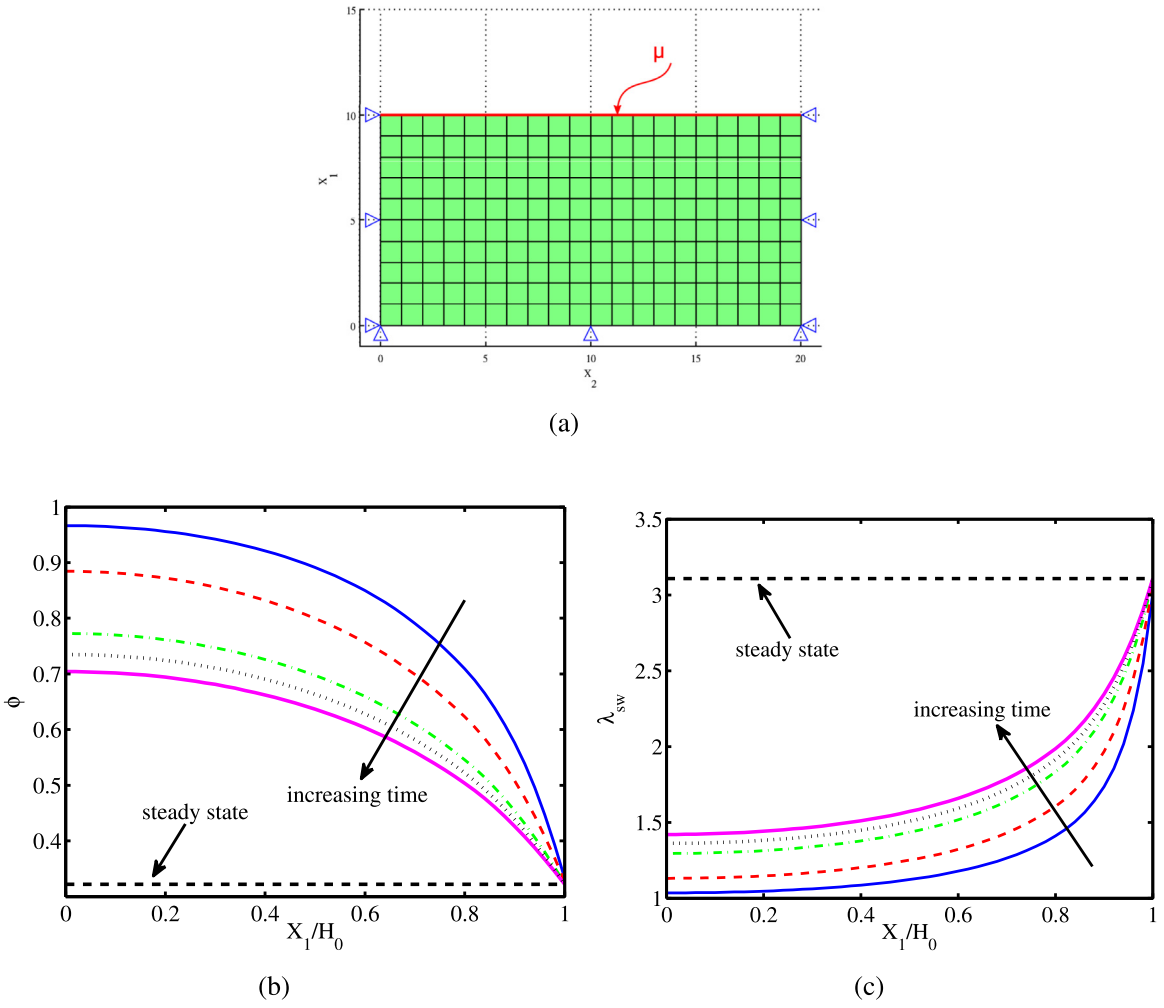

Fig. 3. Transient free-swelling response of 1D gel sheet: (a) the initial setup, (b) the polymer volume fraction ϕ, and (c) the inelastic stretch λ_{sw} w.r.t. the normalized coordinate in X_1-direction.

the time evolution are shown in Fig. 4. The contour plots of the polymer volume fraction ϕ are also plotted in the same figure to provide a physical intuition of the swelling process.

Inverse analysis is then conducted using the experiment-like data corresponding to the target shape shown in Fig. 6(c). The regularized parameter β is obtained from the residual L-curve. The optimal value of β is chosen at the corner point on the curve, see Fig. 5. The convergences of the objective function and the L^2 error norm w.r.t. the iteration are shown in Fig. 6. The reconstructed shape after 25 iterations is illustrated in Fig. 6(d). Good agreement between the numerically identified chemical potential $\mu^{\text{inv}} = -14398$ J and the desired value $\mu^{\text{tar}} = -14392$ J resulting in the target shape can be realized. We have examined the two different probability density functions (PDFs) representing the two different random noise vectors, i.e. $\boldsymbol{\eta}_1 \in [-0.5, 0.5]$ and $\boldsymbol{\eta}_2 \in [-1, 1]$. The obtained results in Fig. 6(a+b) show that the convergences of the objective function and the L^2 error norm w.r.t. the number of iterations are independent of the PDF used to model the random noise. Furthermore, we have used another perturbation value 5×10^{-3}. The convergence of the objective function and the L^2 error norm w.r.t. iteration steps are shown in Figs. 6(c+d). It can be concluded that the convergence is independent of the perturbation value.

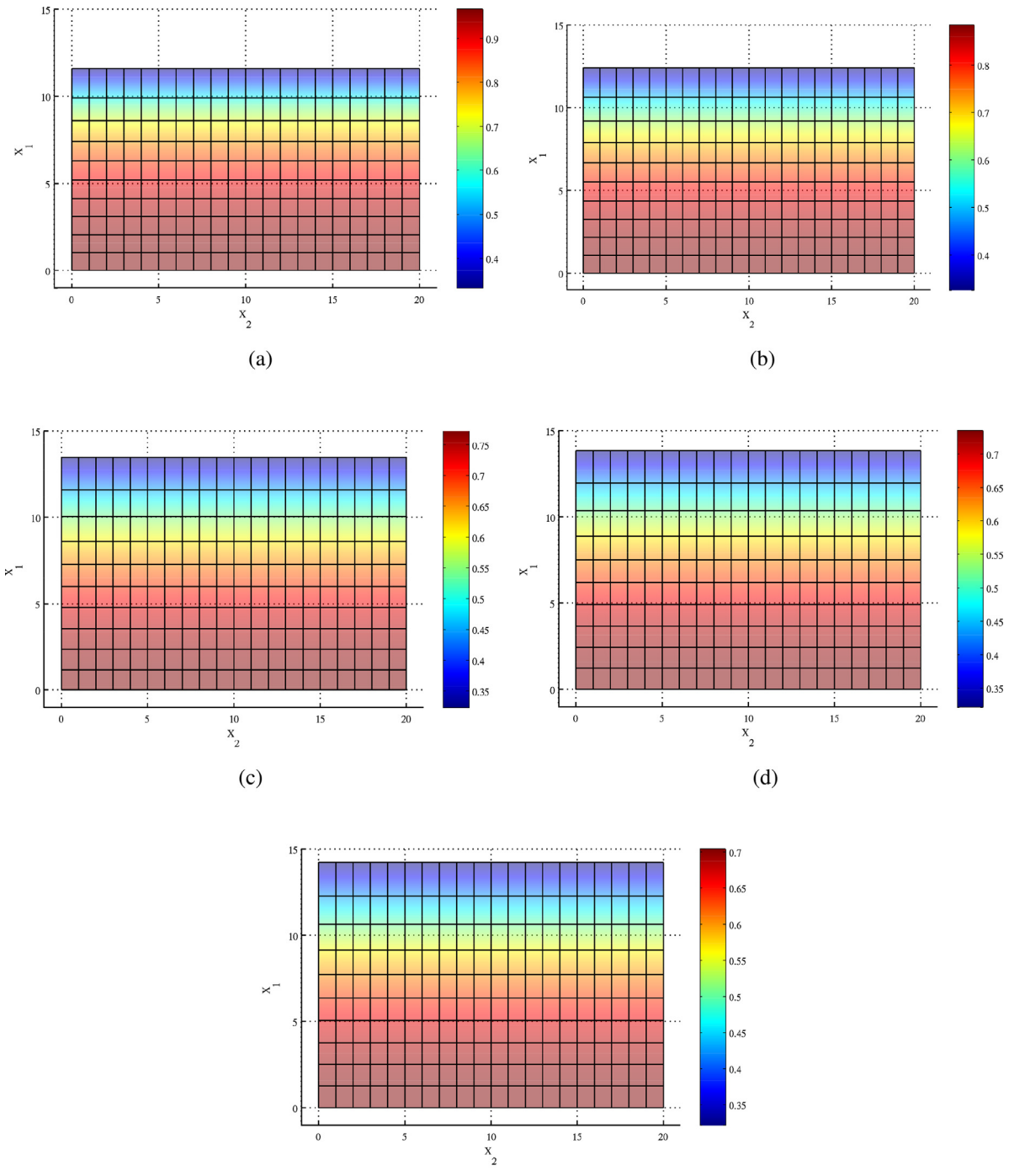

Fig. 4. Transient free-swelling response of 1D gel sheet: the deformed structure after (a) 1 h, (b) 2 h, (c) 4 h, (d) 5 h, and (e) 6 h of free swelling. The contour plots of the polymer volume fraction ϕ are shown on the deformed structure at different instances of time.

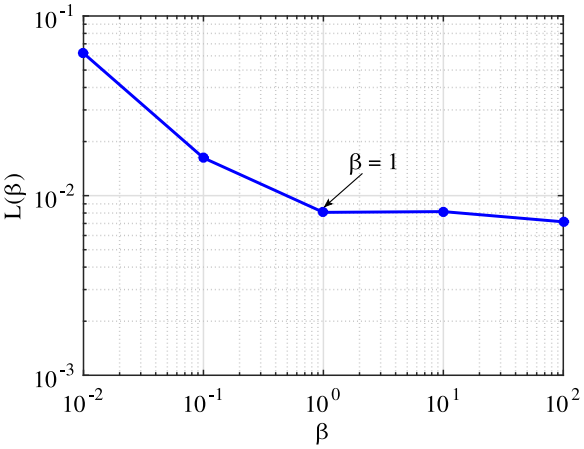

Fig. 5. Transient free-swelling response of 1D gel sheet: Residual L-curve represents the objective function versus the regularization parameter β.

9.2. Two-dimensional transient swelling

In the next example, we examine the transient free-swelling of two-dimensional polymer gel sheet. The problem setup is described in Fig. 7. Since the model is symmetric about the x- and y-axes, a quarter of the sheet (ABCD) is simulated by a quadratic NURBS mesh consisting of 10×10 elements. All FE nodes on the edge AB are fixed in X_1-direction while all FE nodes along the edge AD are fixed in X_2-direction to ensure the symmetry constraint. The edges BD and CD are traction-free and they are prescribed by a zero fluid flux. The edges BD and CD are in contact with the solvent and the chemical potential is prescribed in the same manner as presented in Eq. (107). The incompressible Neo-Hookean model with the material properties $G_{\text{shear}} = 0.1$ MPa, $\nu = 0.5$, $\Omega = 1 \times 10^{-4}$ m^3/mol, $D = 5 \times 10^{-9}$ m^2/s, $\chi = 0.1$ being adopted. $\phi = 0.9999$ is taken at the dry state.

Plots of the volume fraction and the inelastic stretch w.r.t the normalized x-coordinate at different instances of time are illustrated in Fig. 7. The results show that the volume fraction and the inelastic stretch tend to approach the equilibrium values $\phi_{\text{eq}} \approx 0.2870$ and $\lambda_{\text{eq,sw}} \approx 3.4848$ at the steady state.

Contour plots of the polymer volume fraction ϕ on the deformed shape over the time history are illustrated by Figs. 8. The swelling process can be described as follows: (1) at first the area near the corners is swollen faster due to the arisen fluid flux from the two outermost surfaces, see Fig. 8(a); (2) over time the middle is swollen and the square shape is fulfilled gradually as shown from Fig. 8(b) to Fig. 8(d). It is noted that the swelling process shows the same behavior as the one shown in [15].

Having obtained the experiment-like data from the target shape shown in Fig. 8(e), we then find the inverse solution. Again, the L-curve is plotted in Fig. 9 from which the optimal regularization parameter $\beta = 1$ 1/J can be determined. Convergence histories of the objective function and the L^2 error norm over iterations are described in Fig. 10(a,b), respectively. The inverse solution $\mu^{\text{inv}} = -14412$ J is obtained after 20 iterations that is in good agreement with the initial value $\mu^{\text{tar}} = -14392$ J used to obtain the measured data. The corresponding shape resulting from the inverse solution is indicated in Fig. 10(d), while the target shape is shown in Fig. 10(c).

9.3. Simply supported curved beam is in contact with the solvent

Next, transient swelling of a simply supported curved beam with $L \times W \times T = 20$ mm $\times$ 10 mm $\times$ 1 mm shown in Fig. 11(a) is studied. The curvature in vertical direction represented by $\delta = 0.25$ mm is chosen in the dry state. The material parameters are adopted similarly to the first two examples. The mesh consists of 20×10 elements. The two ends of the beam are in contact with the solvent and fluid flux-free. The time evolution of the chemical potential $\mu(t)$, Eq. (107), is applied at the boundaries for chemical potential.

The volume fraction and the inelastic stretch as functions of the normalized coordinates X_1/L are plotted in Fig. 11. The equilibrium values $\phi_{\text{eq}} \approx 0.3666$ and $\lambda_{\text{eq,sw}} \approx 2.7277$ are obtained at the steady state. It can be seen

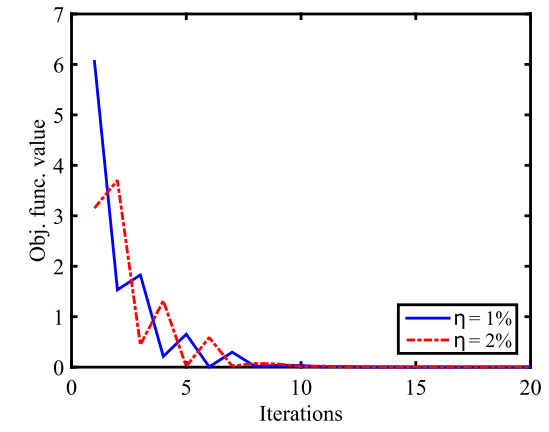

(a)

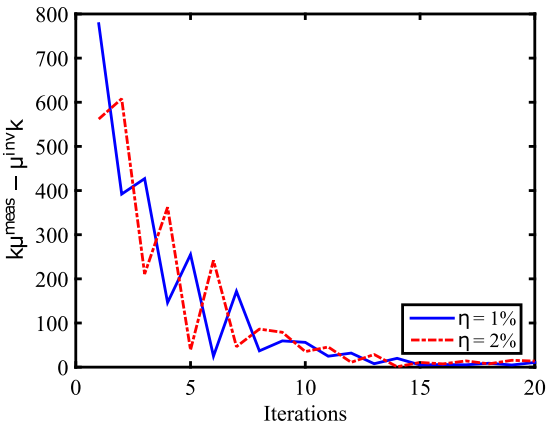

(b)

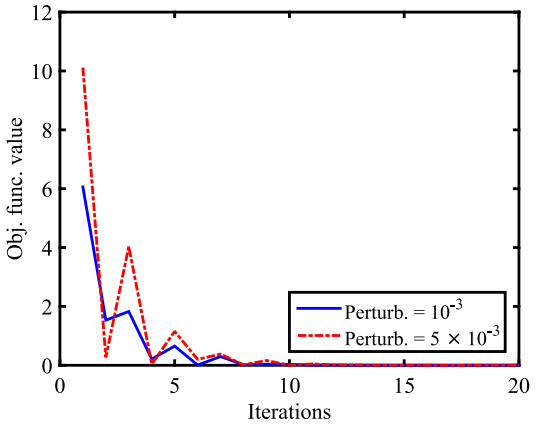

(c)

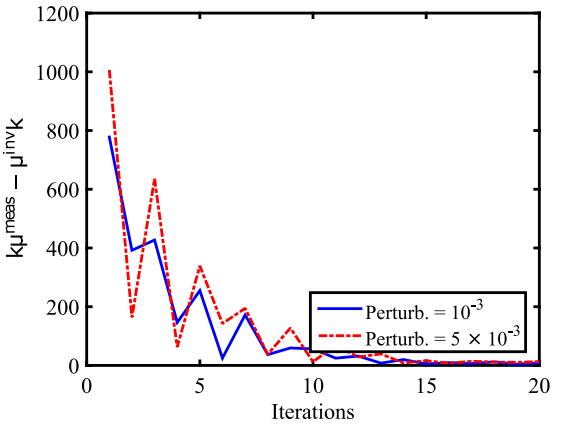

(d)

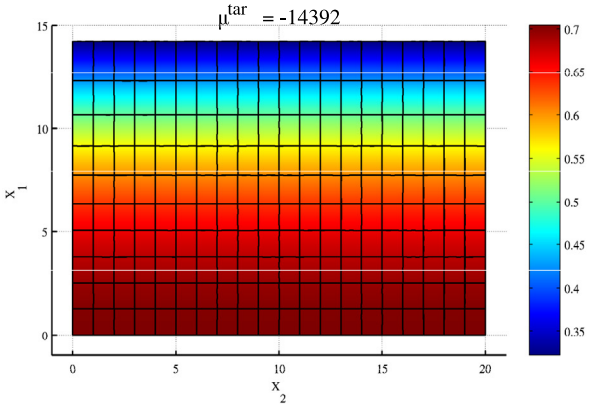

(e)

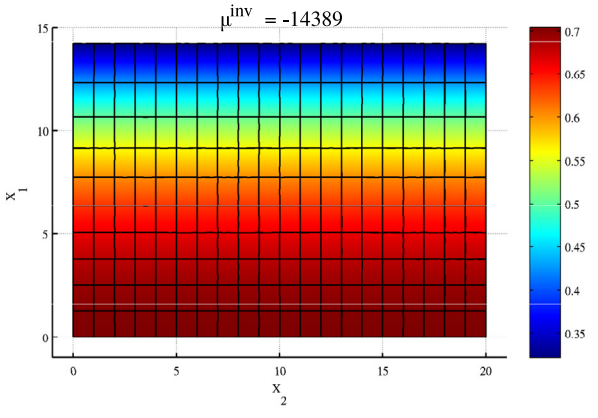

(f)

Fig. 6. Transient free-swelling response of 1D gel sheet: Convergence of (a) the objective function, and (b) L^2 error norm during optimization process, (c) the target shape, (d) the reconstructed shape at the final iteration.

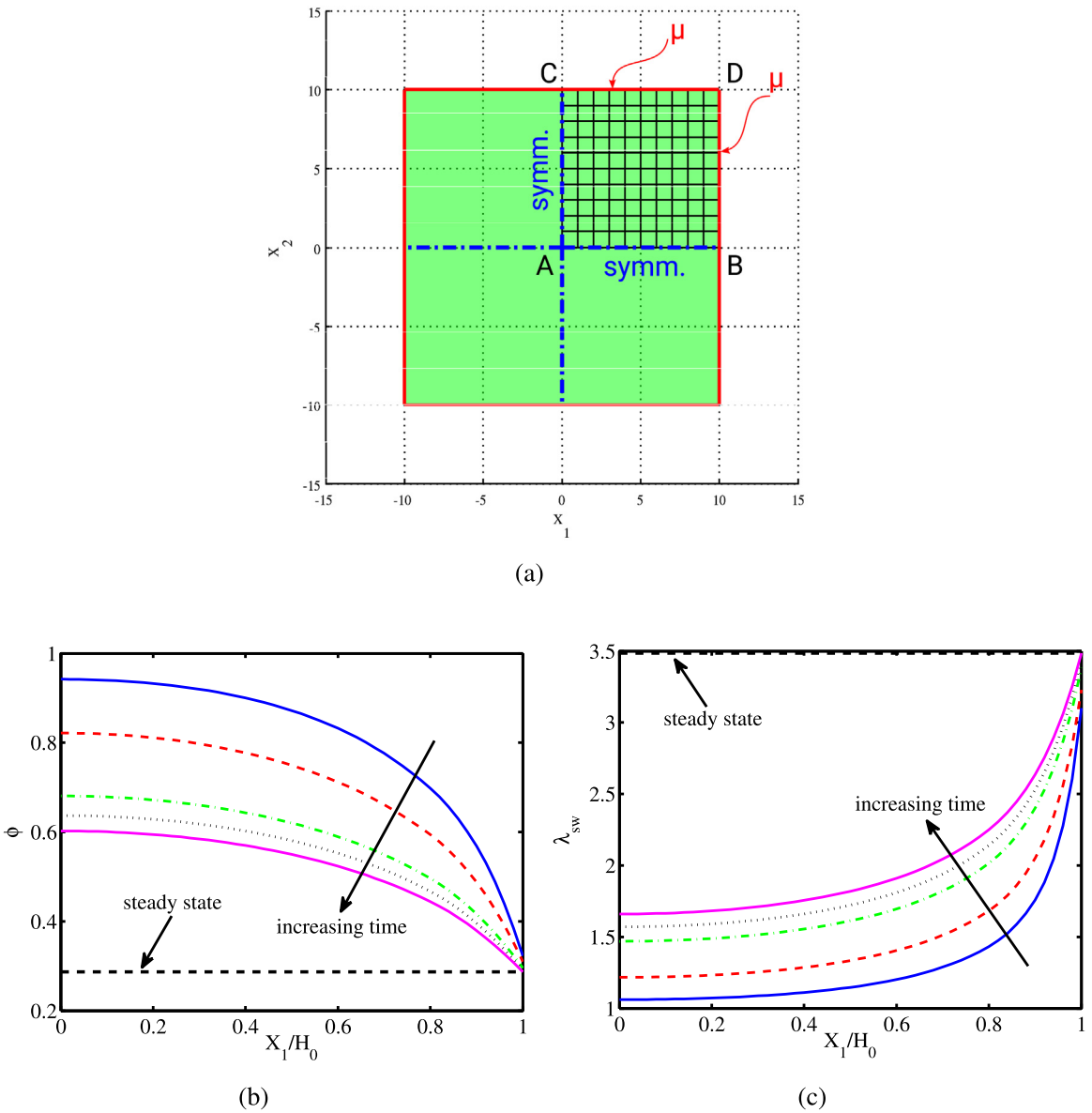

Fig. 7. Transient free-swelling response of 2D gel sheet: (a) the initial setup; (b) the polymer volume fraction ϕ, and (c) the inelastic stretch λ_{sw} w.r.t. the normalized coordinate in X_2-direction.

that the curved beam has been buckled under solvent stimulation. The swelling-induced deformations of the beam at different instances of time are shown in Fig. 12.

The chemical potential value needed to generate the target shape shown in Fig. 12(f) is then identified via the inverse analysis. The residual L-curve is plotted in Fig. 13 whose corner point refers the optimal regularization parameter $\beta = 0.1$ 1/J. As shown in Fig. 13, the objective function and the L^2 error norm are converged after 25 iterations. Accordingly, the inverse solution $\mu^{\text{inv}} = -14406$ J is obtained that agrees well with the initial value $\mu^{\text{tar}} = -14392$ J prescribed to generate the target shape. The resulting shape, see Fig. 14(b), is then reconstructed that is almost identical to the target shape shown in Fig. 14(a).

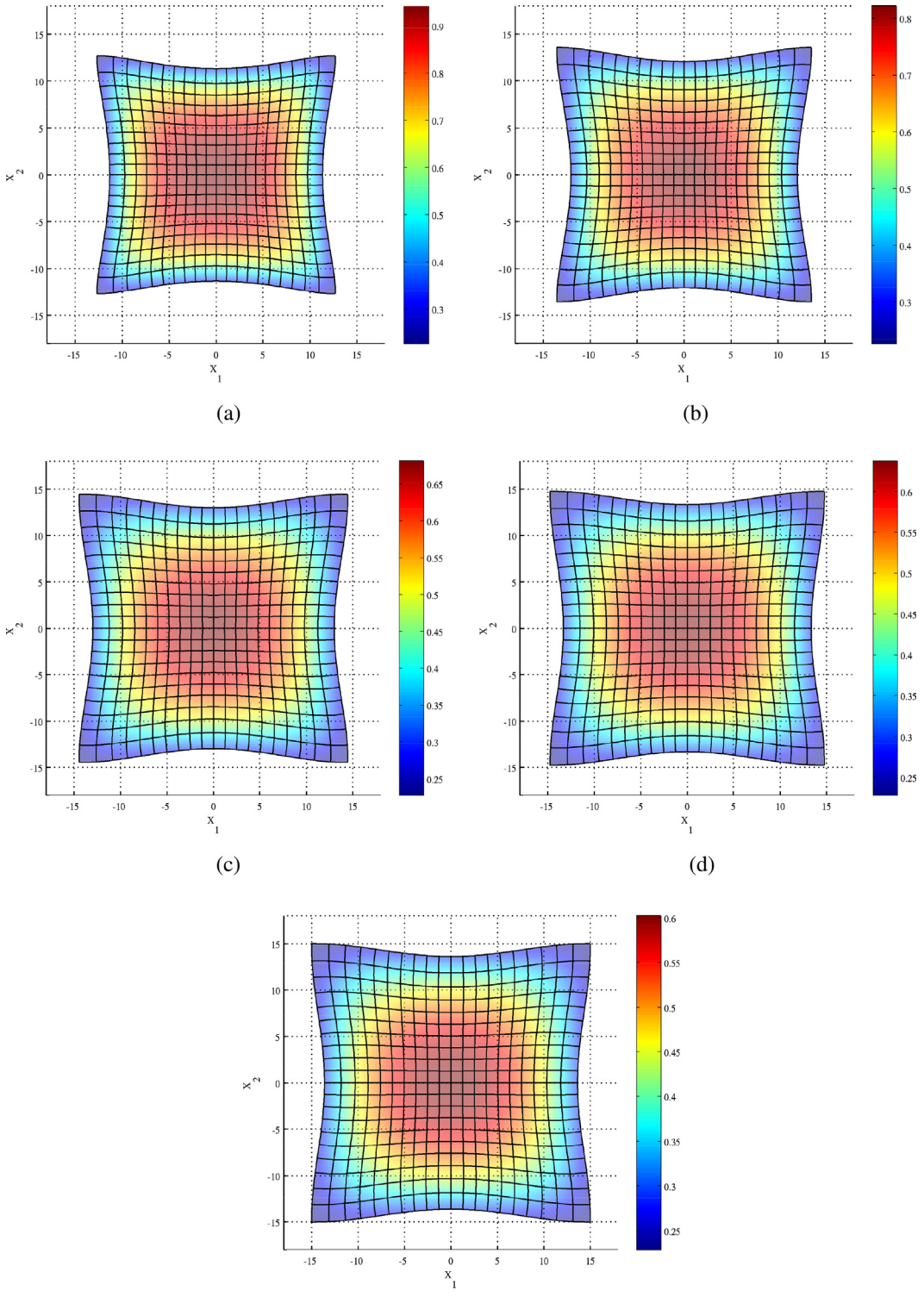

Fig. 8. Transient free-swelling response of 2D gel sheet: the deformed structure after (a) 1 h, (b) 2 h, (c) 4 h, (d) 5 h, and (e) 6 h of free swelling. The contour plots of the polymer volume fraction ϕ are shown on the deformed structure at different instances of time.

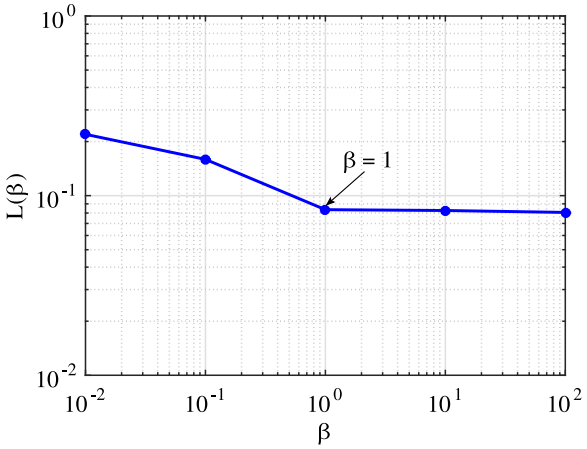

Fig. 9. Transient free-swelling response of 2D gel sheet: Residual L-curve represents the objective function value versus the regularization parameter β.

9.4. Dome-shaped disk subjected to the combination of solvent stimulation and a prescribed displacement at the center

The final example studies transient swelling of a circular disk. The geometrical and material parameters, radius $R = 10$ mm, thickness $T = 1$ mm, shear modulus $G_{\text{shear}} = 0.1$ MPa, Poisson's ration $\nu = 0.5$ and the solvent molecule $\Omega = 1 \times 10^{-4}$ m^3/mol are taken. The remaining parameters are taken as $D = 5 \times 10^{-9}$ m^2/s, $\chi = 0.1$, respectively. The disk is clamped at the outermost boundary which is in contact with the solvent while a zero fluid flux is prescribed. The chemical potential approaches μ^0 follows Eq. (107). The computational domain is discretized using 16×16 quadratic, C^1-continuous NURBS elements as depicted in Fig. 15(a). As a consequence, C^1-continuity has been lost at the center where the NURBS discretization degenerates, see [56]. Displacement $\boldsymbol{u}$ is prescribed on both the central point and the closest ring of control points around the center. In this way, the tangent plane at the tip is kept horizontally unchanged so that the C^1-continuity is saved.

Fig. 15 shows the buckling of swelling disk. The buckling (elastic softening) of the disk during swelling process can be realized according to the force–displacement curves measure at **B** (the reaction force) and **A** (the displacement) shown in Fig. 15(b). The force–displacement curves correspond to different prescribed displacement at the center, i.e. $u = 3.2$ mm, 3.6 mm and 4 mm, respectively. Furthermore, the transient morphology of the swollen disk after a few different times is shown in Fig. 15

Subsequently, inverse analysis is applied upon the displacement and the chemical potential measured from the target shape. The optimally regularized parameter for the out-of-plane displacement $\beta = 10^3$ 1/mm is obtained from the corresponding L-curve shown in Fig. 16. Convergent solutions of the chemical potential and the out-of-plane displacement are obtained after 25 optimization steps. The solutions, i.e. the applied chemical potential $\mu^{\text{inv}} = -14388$ J and the out-of-plane displacement $u^{\text{inv}} = 1.796$ mm are identified inversely. The resulting shape is shown in Fig. 17(b). Obviously, the reconstructed shape is in agreement with the target shape shown in Fig. 17(a).

9.5. Dome-shaped disk subjected to the combination of solvent stimulation and a lateral disturbing pressure

In this example, transient swelling of a geometric composite disk composed of an inner circular disk and an outer annulus is modeled. The respective outer annulus radii are taken as $R_i = 5$ mm and $R_e = 12$ mm and the inner radius $r = 5$ mm is chosen in the dry state. These sizes make them compatible each other without pre-stretch. The thickness $h = 1$ mm of both the disk and the annulus is designed. The material properties of the incompressible Neo-Hookean model are taken similarly to those used in the fourth example. The geometry is composed of nine Bézier patches numerically. To fulfill C^1-continuity at the patch interfaces, Lagrange multiplier method presented in [30,31] is employed. The geometry, boundary conditions and discretized mesh are described in Fig. 18(a). The outermost boundary of the composite disk is in contact with the solvent while a zero fluid flux is prescribed so that

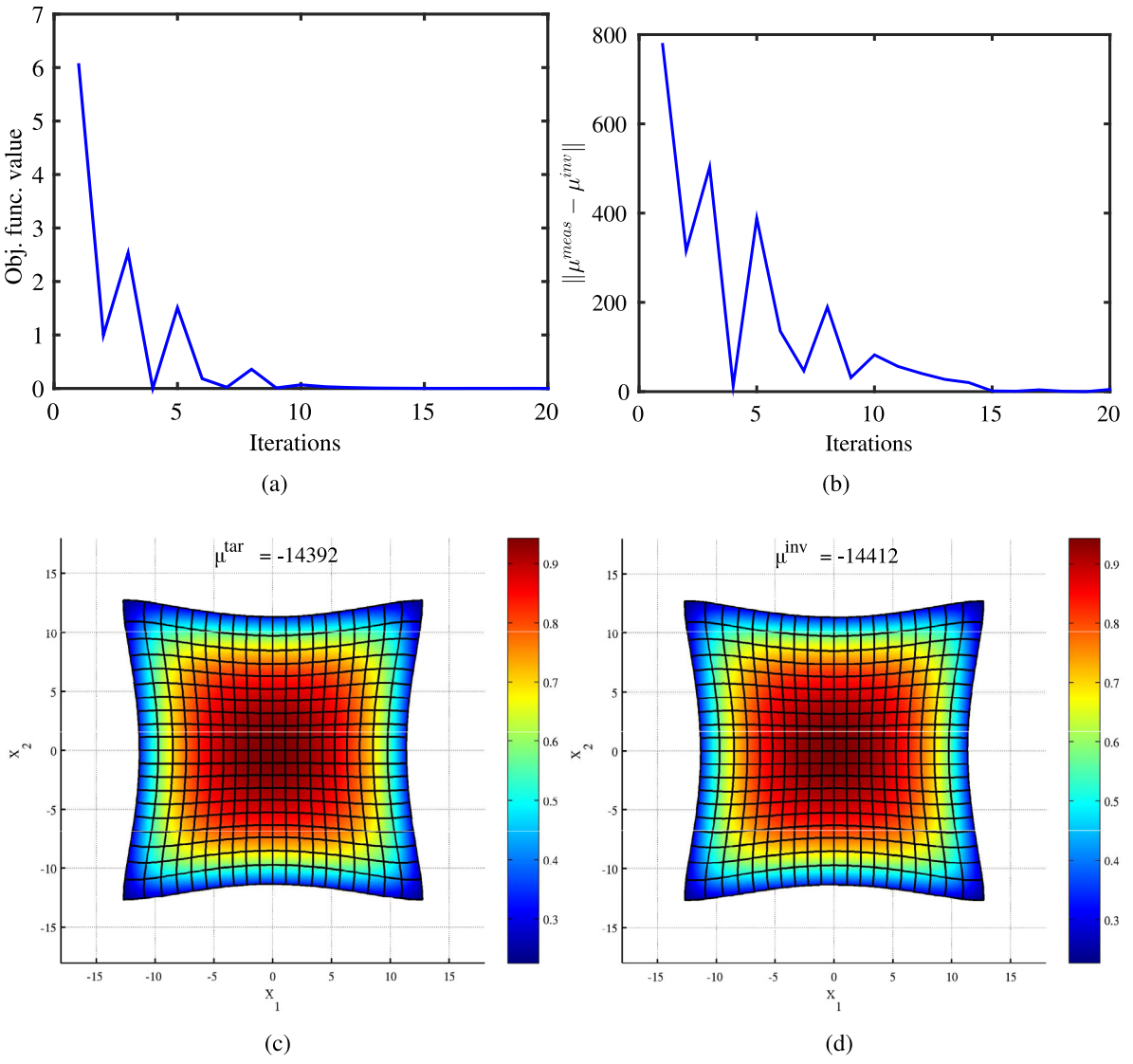

Fig. 10. Transient free-swelling response of 2D gel sheet: Convergence of (a) the objective function, and (b) L^2 error norm during optimization process, (c) the target shape, (d) the reconstructed shape at the final iteration.

the chemical potential approaches μ^0 following Eq. (107). A lateral pressure $q = 5 \times 10^{-3}$ N/mm^2 is applied on the inner disk during the swelling process to mimic load imperfection occurring in reality.

The swelling-induced deformations of the disk are shown in Fig. 18 at different time steps. Buckling behavior (elastic softening) is also shown by the reaction force measured at **B** versus the displacement of the center **A** in Fig. 18(b).

Inverse analysis using the displacement and the chemical potential resulting from the target shape represented by Fig. 18(f) is employed to determine the chemical potential applied on the boundary and the lateral pressure. Making use the L-curve plot, see Fig. 19, we can obtain the optimal regularization parameter for the lateral pressure $\beta = 5 \times 10^9$ mm^2/N. Figs. 20(a–b) show the convergence histories of the objective function and the L^2 error norm over the iterations. The optimal solutions which are the prescribed chemical potential $\mu^{\text{inv}} = -14408$ J and the lateral pressure $q^{\text{inv}} = 1.0007 \times 10^{-6}$ N/mm^2 are solved inversely. After 20 iterations, the corresponding observed in Fig. 20(d) shows excellent agreement with the target shape depicted by Fig. 20(c).

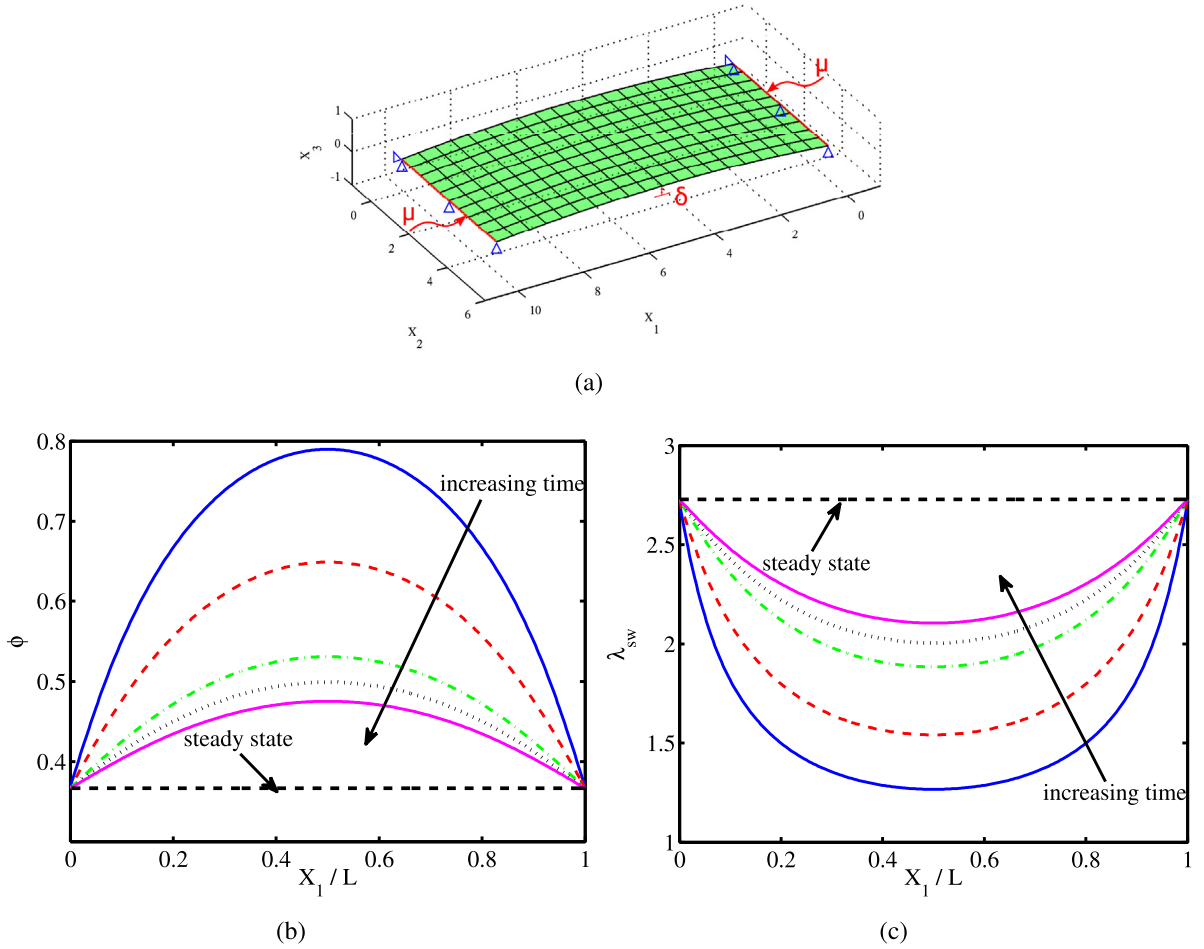

Fig. 11. Transient free-swelling response of simply supported beam: (a) the initial setup, (b) the polymer volume fraction ϕ, and (c) the inelastic stretch λ_{sw} w.r.t. the normalized coordinate in X_1-direction.

10. Conclusion

Hydrogels are one of the most widely studied and investigated forms of stimuli-responsive soft matter. Furthermore, it has been a challenge to identify the external loads and stimuli that are required to actuate these complex materials to achieve desired 3D forms. To resolve this, we have developed a novel formulation that, by utilizing both nonlinear kinematics and material models, captures the coupling between elasticity and solvent transport using an isogeometric analysis-based numerical discretization of Kirchhoff–Love shell theory. Second, we developed a novel inverse methodology that chemomechanically couples large deformation and mass transport to identify the external stimuli prescribed to generate a specific target shape. We use these new formulations to study the shape morphing of 2D thin sheets to 3D shapes driven by swelling, which is governed by the coupling between mass transport and large deformation. By being based on nonlinear field theories, the formulation is able to describe the swelling induced morphing of responsive materials from 2D flat shells to 3D curved shapes involving instabilities/elastic softening. Furthermore, the numerical examples involving the inverse analysis based isogeometric analysis were shown to accurately identify the prescribed external stimuli required to reconstruct a specific target shape. As a result, this formulation can play a role in enabling the design and analysis of user-defined stimuli-responsive soft matter.

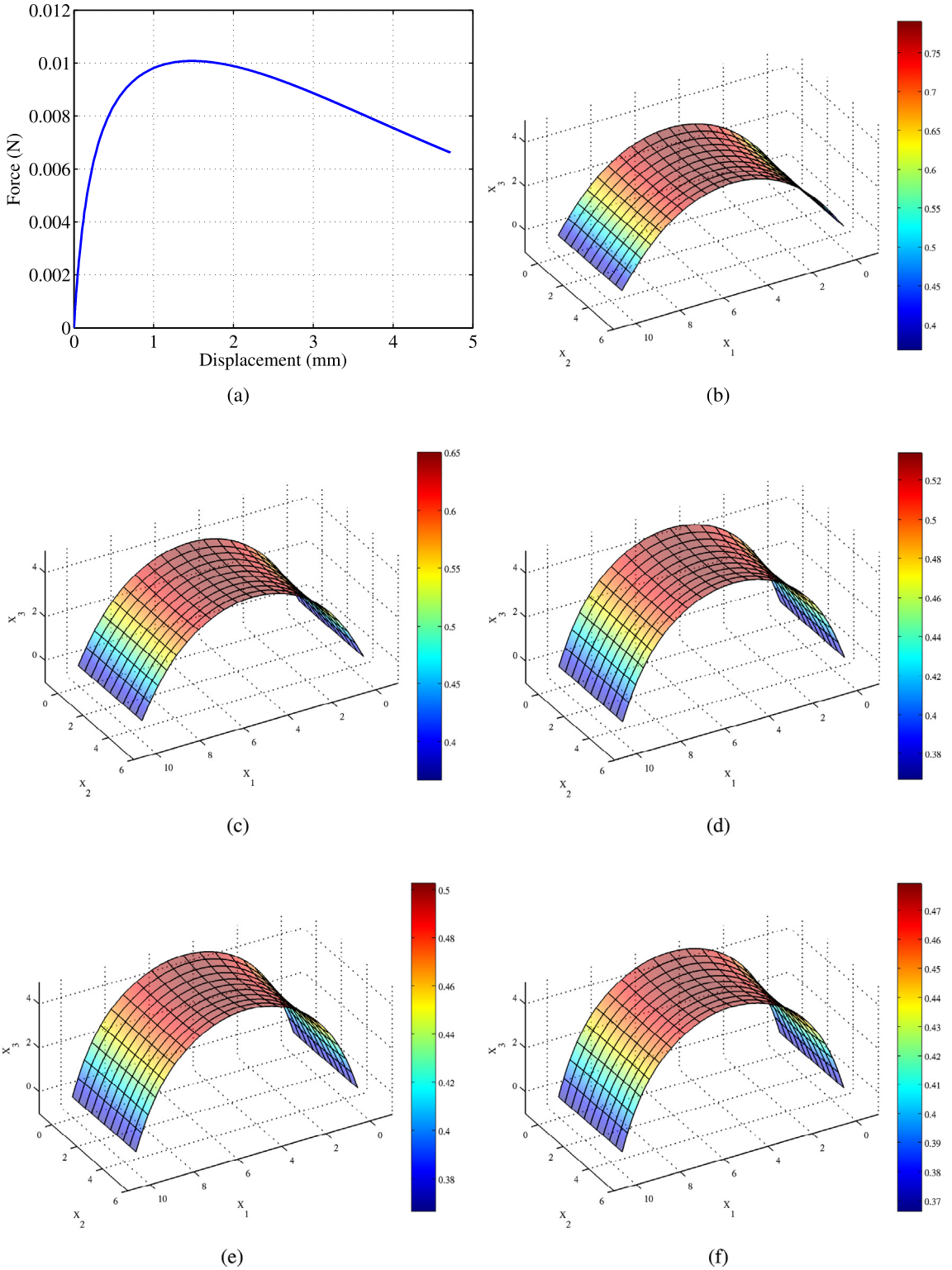

Fig. 12. Transient free-swelling response of simply supported beam: the contour plots of the polymer volume fraction ϕ shown on the deformed structure at (a) 1 h, (b) 2 h, (c) 4 h, (d) 5 h, and (e) 6 h of free swelling.

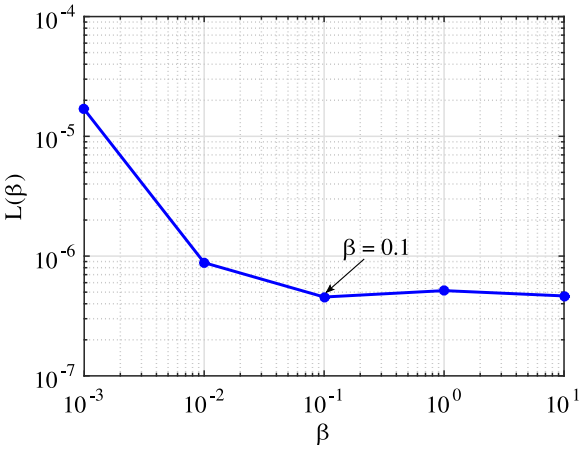

Fig. 13. Transient free-swelling response of simply supported beam: Residual L-curve represents the objective function versus the regularization parameter β.

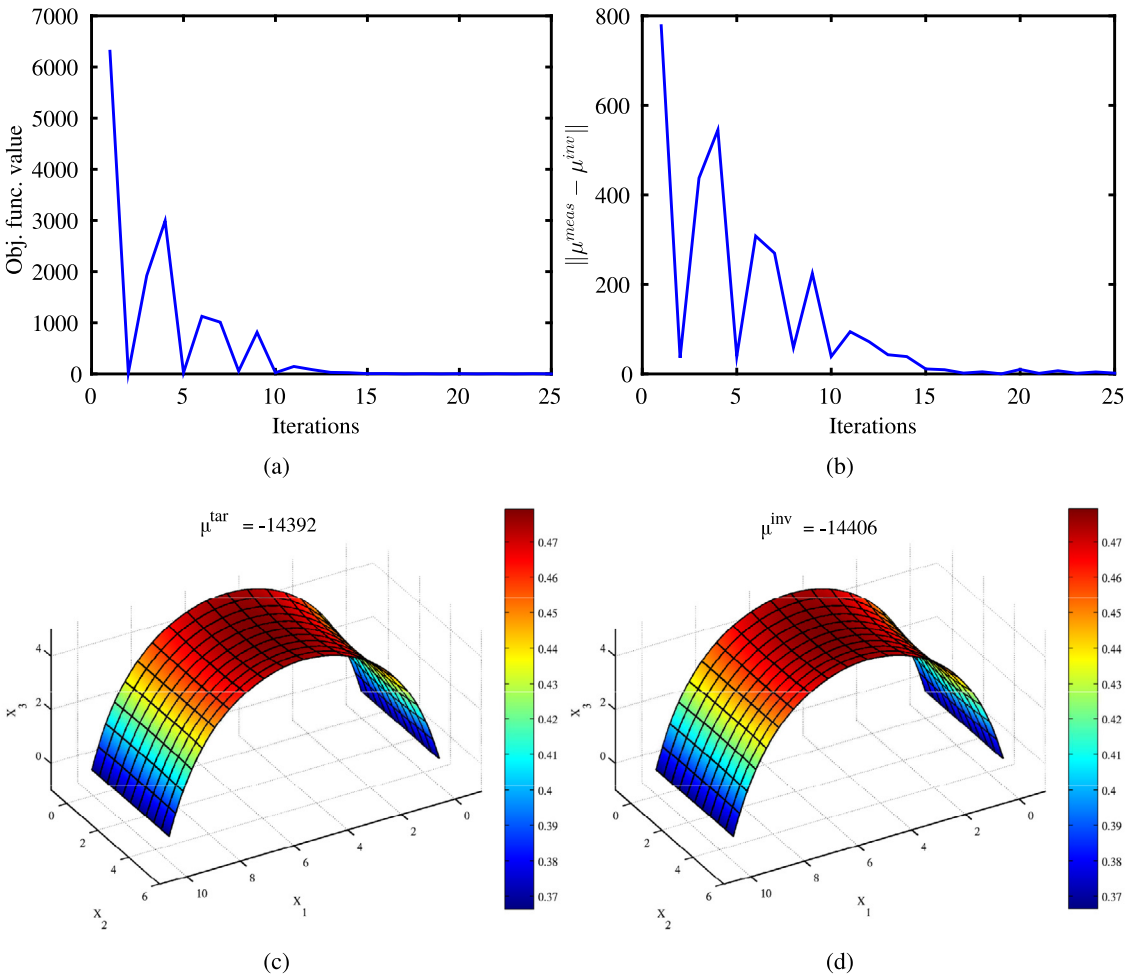

Fig. 14. Transient free-swelling response of simply supported beam: Convergence of (a) the objective function, and (b) L^2 error norm during optimization process, (c) the target shape, (d) the reconstructed shape at the final iteration.

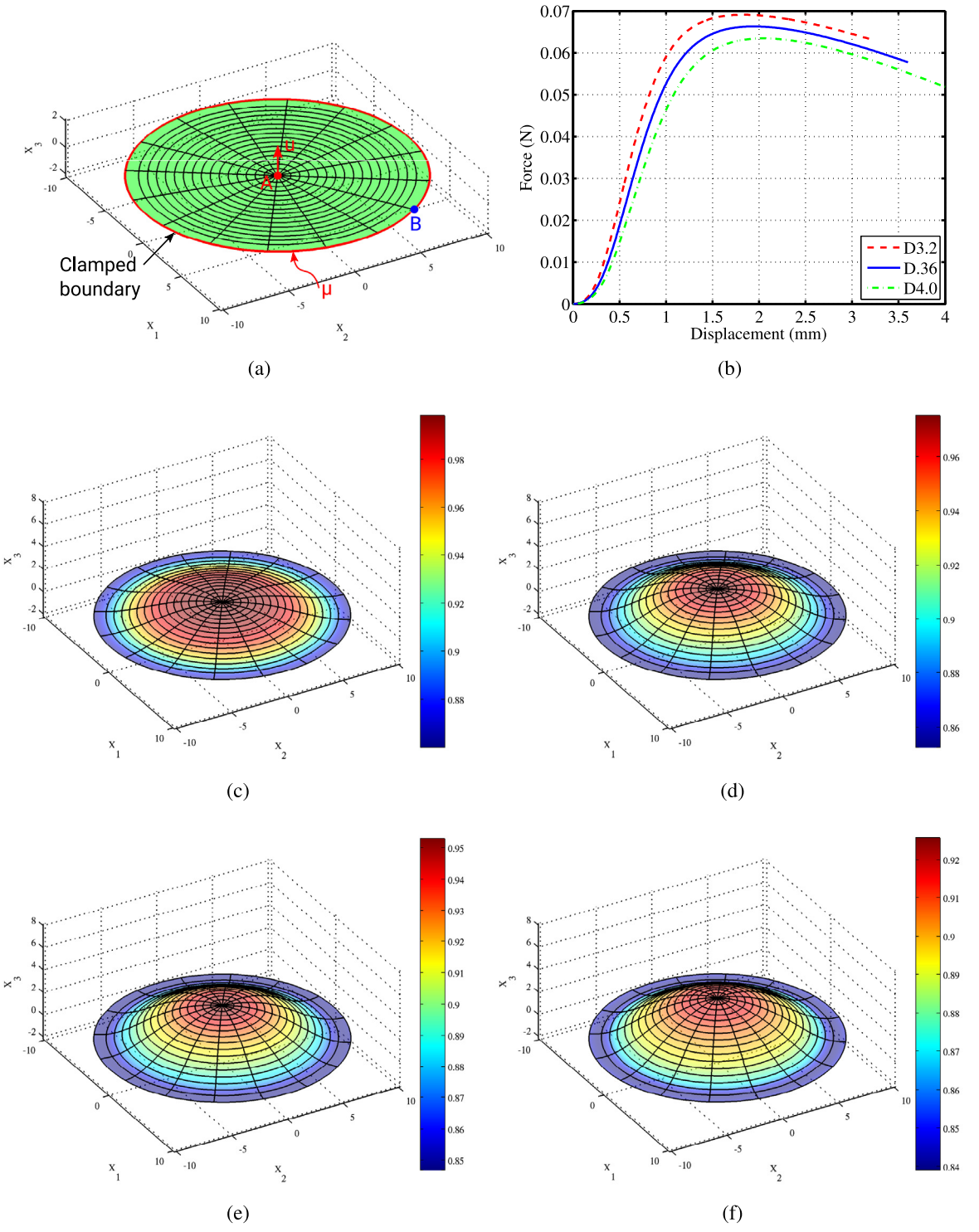

Fig. 15. Disk is subjected to the combination of solvent stimulation and a vertical displacement at the center: (a) the initial setup, (b) the force–displacement curves corresponding to different prescribed displacement u at the center **A**, and (c) the contour plots of the polymer volume fraction ϕ shown on the deformed structure at (c) 20 min, (d) 40 min, (e) 50 min, and (f) 1 h.

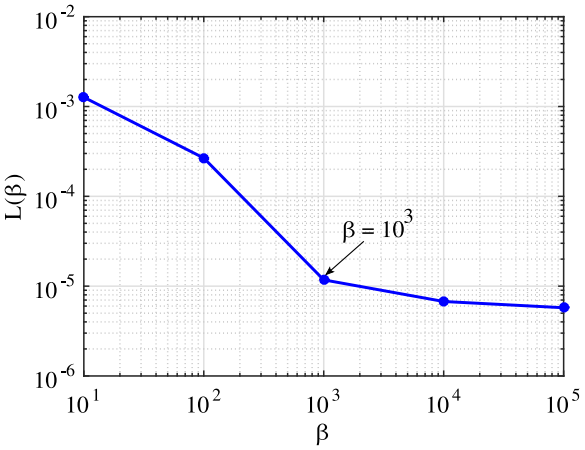

Fig. 16. Disk is subjected to the combination of solvent stimulation and a vertical displacement at the center: Residual L-curve represents the objective function value versus the regularization parameter β.

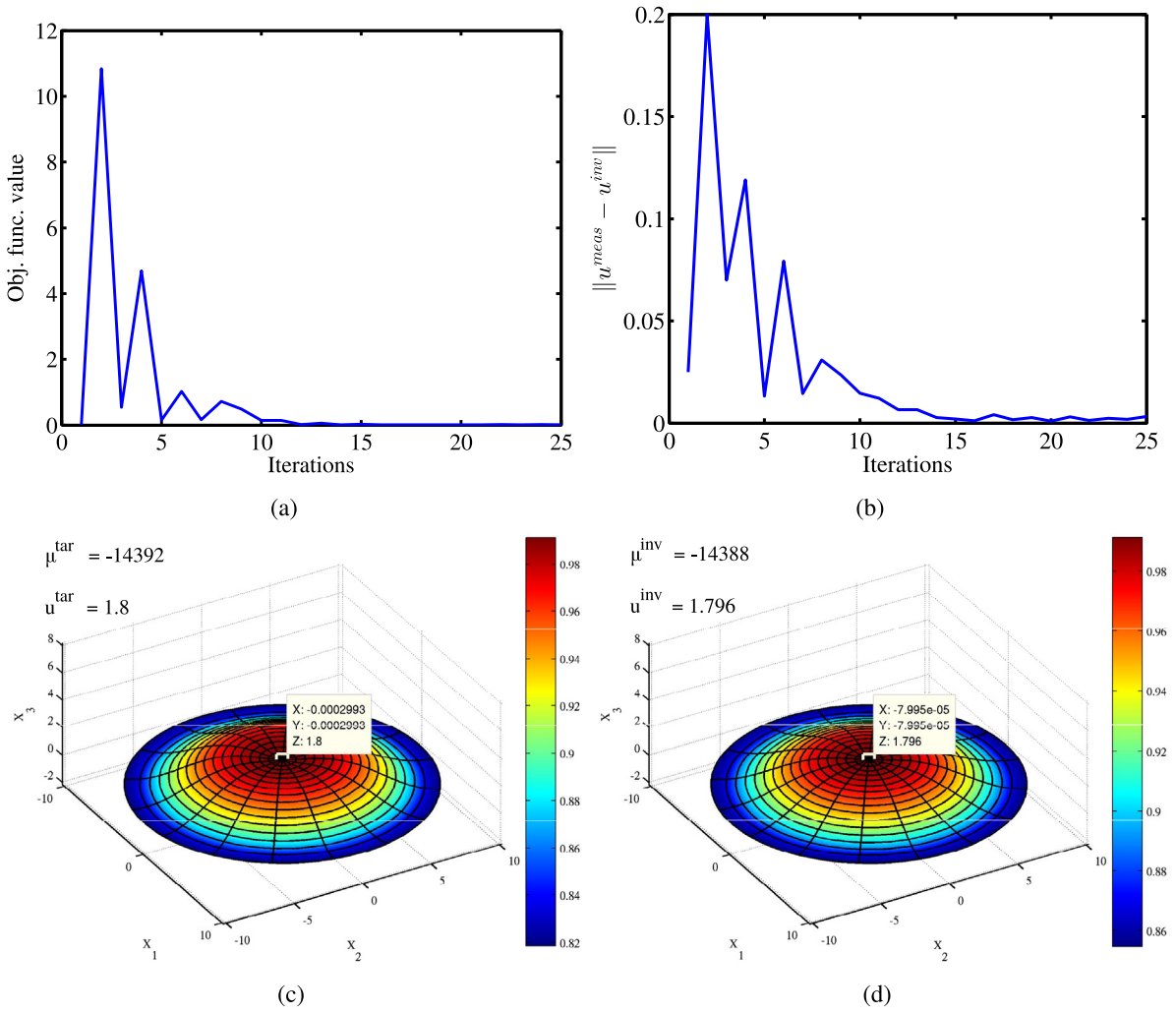

Fig. 17. Disk is subjected to the combination of solvent stimulation and a vertical displacement at the center: Convergence of (a) the objective function, and (b) L^2 error norm during optimization process, (c) the target shape, (d) the reconstructed shape at the final iteration.

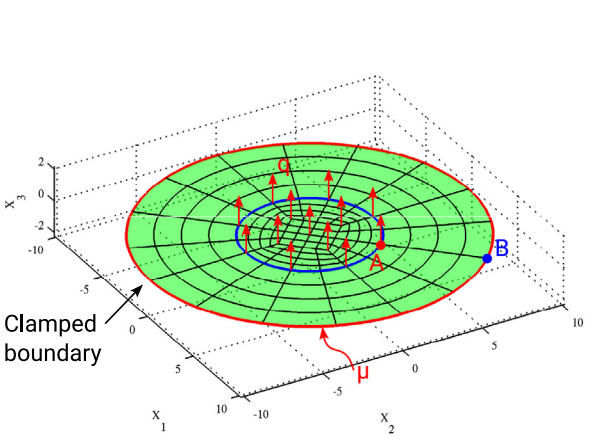

(a)

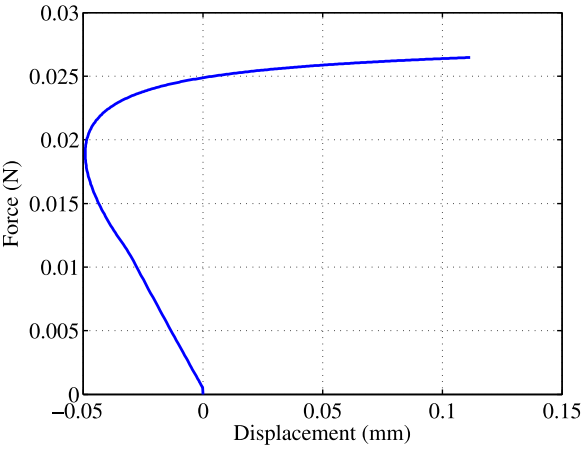

(b)

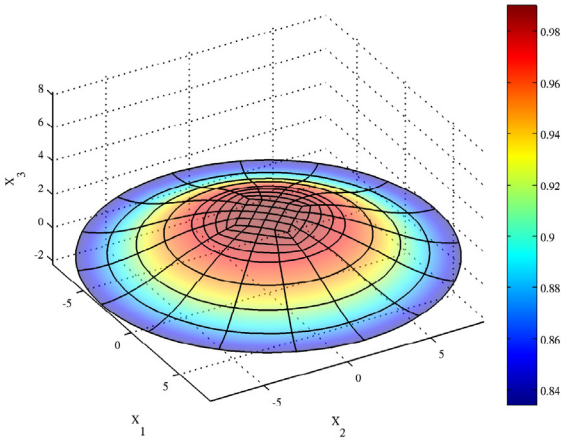

(c)

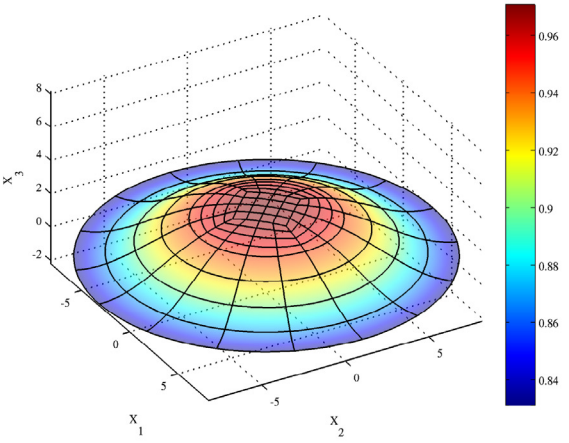

(d)

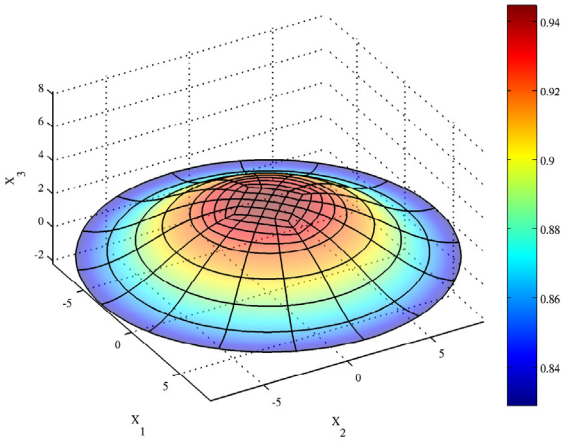

(e)

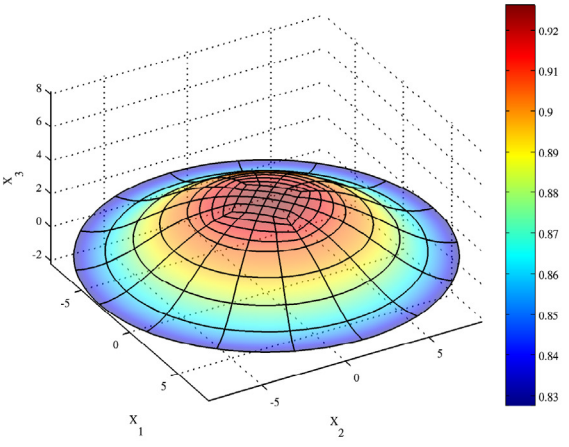

(f)

Fig. 18. Disk is subjected to the combination of solvent stimulation and a lateral disturbing pressure: (a) the initial setup, (b) the force–displacement curve, and the contour plots of the polymer volume fraction ϕ shown on the deformed structure at (c) 30 min, (d) 40 min, (e) 50 min, (f) 1 h.

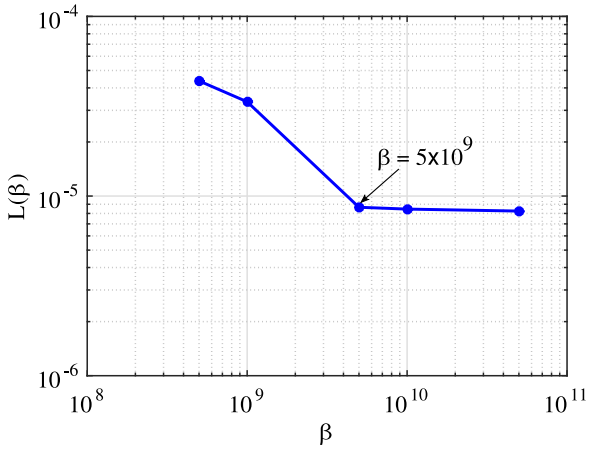

Fig. 19. Disk is subjected to the combination of solvent stimulation and a lateral disturbing pressure: Residual L-curve represents the objective function value versus the regularization parameter β.

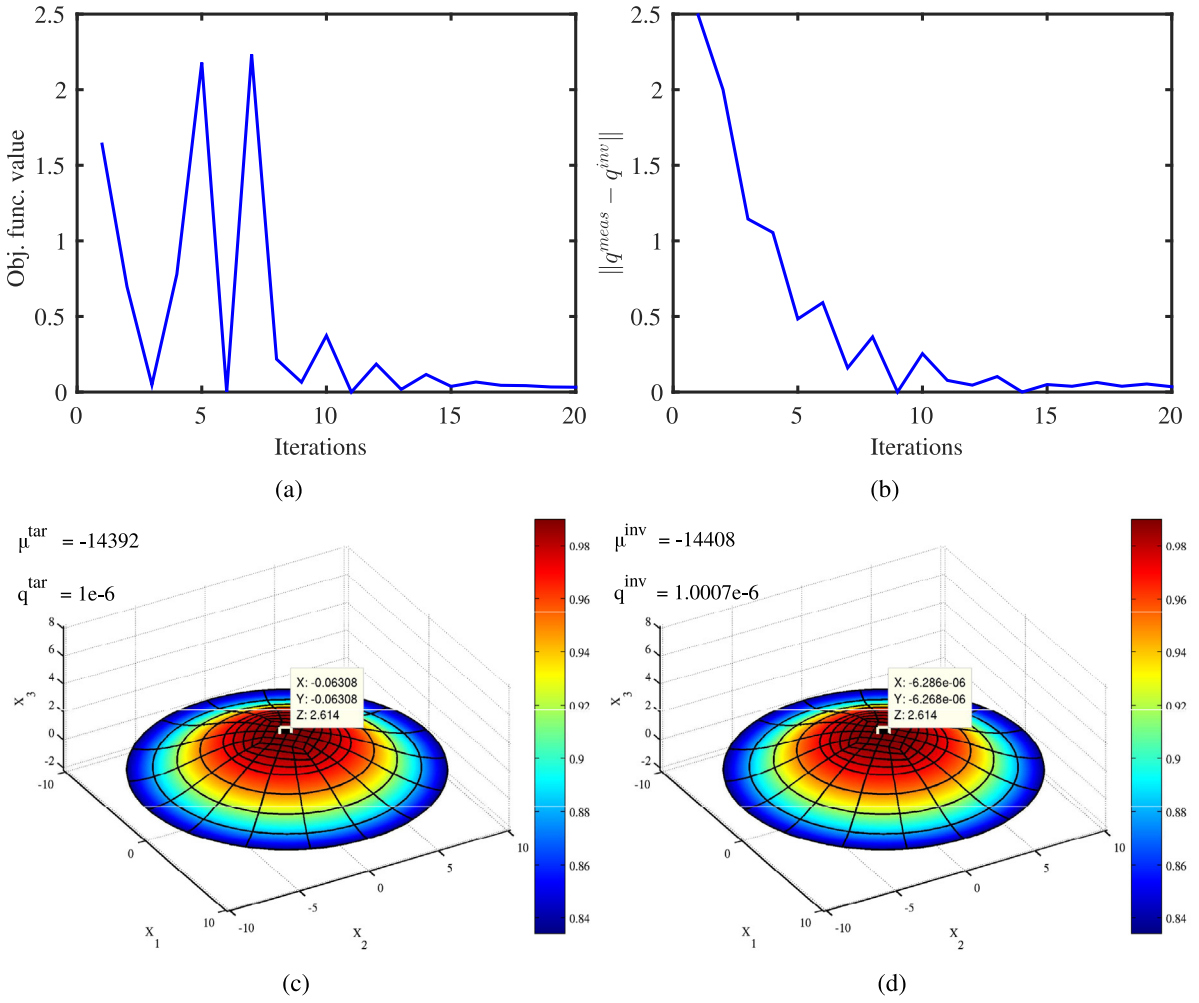

Fig. 20. Disk is subjected to the combination of solvent stimulation and a lateral disturbing pressure: Convergence of (a) the objective function, and (b) L^2 error norm during optimization process, (c) the target shape, (d) the reconstructed shape at the final iteration.

Declaration of competing interest

The authors declare that they have no known competing financial interests or personal relationships that could have appeared to influence the work reported in this paper.

Acknowledgments

The authors gratefully acknowledge the support of the ERC Starting Grant (802205) from European Union and the Deutsche Forschungsgemeinschaft (DFG, German Research Foundation) under Germany's Excellence Strategy within the Cluster of Excellence PhoenixD (EXC 2122, Project ID 390833453). Professor Krister Svanberg from Royal Institute of Technology is acknowledged gratefully for providing the MMA code used in this study.

Appendix. Linearization of kinematical quantities

A.1. Linearization of $\tilde{\boldsymbol{a}}_\alpha$ and $\tilde{\boldsymbol{a}}^\alpha$ in the direction $\Delta\mu$

From Eq. (23), we thus arrive

$$\begin{aligned}\Delta_\mu \tilde{\boldsymbol{a}}_\alpha &= -\frac{1}{2}\phi^{-3/2}\boldsymbol{A}_\alpha \frac{\partial\phi}{\partial\mu}\Delta\mu,\\ \Delta_\mu \tilde{\boldsymbol{a}}^\alpha &= \frac{1}{2}\phi^{-1/2}\boldsymbol{A}^\alpha \frac{\partial\phi}{\partial\mu}\Delta\mu.\end{aligned} \tag{A.1}$$

A.2. Linearization of $\tilde{a}_{\alpha\beta}$, $\tilde{a}^{\alpha\beta}$ and $\tilde{b}_{\alpha\beta}$, $\tilde{b}^{\alpha\beta}$ in the direction $\Delta\mu$

Using Eqs. ((4).1) and ((17).1), we have

$$\tilde{a}_{\alpha\beta} = J_{\text{sw}}\, A_{\alpha\beta} = \frac{1}{\phi}\, A_{\alpha\beta}, \quad \tilde{a}^{\alpha\beta} = \frac{1}{J_{\text{sw}}}\, A^{\alpha\beta} = \phi\, A^{\alpha\beta}. \tag{A.2}$$

The corresponding linearizations of $\tilde{a}_{\alpha\beta}$ and $\tilde{a}^{\alpha\beta}$ take the form

$$\begin{aligned}\Delta_\mu \tilde{a}_{\alpha\beta} &= -\frac{1}{\phi^2}\, A_{\alpha\beta}\, \frac{\partial\phi}{\partial\mu}\Delta\mu,\\ \Delta_\mu \tilde{a}^{\alpha\beta} &= A^{\alpha\beta}\, \frac{\partial\phi}{\partial\mu}\Delta\mu.\end{aligned} \tag{A.3}$$

and

$$\begin{aligned}\Delta_\mu \tilde{b}_{\alpha\beta} &= -\frac{1}{2}\, \phi^{-3/2}\, B_{\alpha\beta}\, \frac{\partial\phi}{\partial\mu}\Delta\mu,\\ \Delta_\mu \tilde{b}^{\alpha\beta} &= \frac{1}{2}\, \phi^{-1/2}\, B^{\alpha\beta}\, \frac{\partial\phi}{\partial\mu}\Delta\mu.\end{aligned} \tag{A.4}$$

A.3. Linearization of J_{sw} in the direction $\Delta\mu$

As shown in Eq. (19), then follows

$$\Delta_\mu J_{\text{sw}} = \frac{\partial J_{\text{sw}}}{\partial\phi}\, \frac{\partial\phi}{\partial\mu}\Delta\mu = -\frac{1}{\phi^2}\, \frac{\partial\phi}{\partial\mu}\Delta\mu, \tag{A.5}$$

A.4. Linearization of $J^\star_{\text{el}}$ in the direction $\Delta\mu$

The change of $J^\star$ in the direction of $\Delta\mu$ can be formulated as

$$\Delta_\mu J^\star_{\text{el}} = \frac{J^\star_{\text{el}}}{2}\left(\tilde{\omega}^{\alpha\beta}_a\, \Delta_\mu \tilde{a}_{\alpha\beta} + \tilde{\omega}^{\alpha\beta}_b\, \Delta_\mu \tilde{b}_{\alpha\beta}\right) \tag{A.6}$$

with

$$\begin{aligned}\tilde{\omega}_a^{\alpha\beta} &:= \xi^2\ \tilde{\kappa}\ \tilde{m}_a\ \tilde{a}^{\alpha\beta} - \xi^2\ \tilde{m}_b\ \tilde{b}^{\alpha\beta} + \tilde{g}_a\ \tilde{g}^{\alpha\beta},\\ \tilde{\omega}_b^{\alpha\beta} &:= -\xi^2\ \tilde{m}_a\ \tilde{\tilde{b}}^{\alpha\beta} + \xi^2\ \tilde{m}_b\ \tilde{a}^{\alpha\beta} + \tilde{g}_b\ \tilde{g}^{\alpha\beta}.\end{aligned} \tag{A.7}$$

where $\tilde{m}_a = \tilde{g}^{\gamma\delta}\tilde{a}_{\gamma\delta}$ and $\tilde{m}_b = \tilde{g}^{\gamma\delta}\tilde{b}_{\gamma\delta}$ are introduced.

A.5. Linearizarion of $\tilde{s}$ in the direction $\Delta\mu$

Linearizing $\tilde{s}$ shown by Eq. (71), we obtain

$$\Delta_\mu\tilde{s} = 2\xi\ \Delta_\mu\tilde{H} + \xi^2\ \Delta_\mu\tilde{\kappa}. \tag{A.8}$$

with

$$\begin{aligned}\Delta_\mu\tilde{H} &= \frac{\partial\tilde{H}}{\partial\tilde{a}_{\alpha\beta}}\ \Delta_\mu\tilde{a}_{\alpha\beta} + \frac{\partial\tilde{H}}{\partial\tilde{b}_{\alpha\beta}}\ \Delta_\mu\tilde{b}_{\alpha\beta}\\ \Delta_\mu\tilde{\kappa} &= \frac{\partial\tilde{\kappa}}{\partial\tilde{a}_{\alpha\beta}}\ \Delta_\mu\tilde{a}_{\alpha\beta} + \frac{\partial\tilde{\kappa}}{\partial\tilde{b}_{\alpha\beta}}\ \Delta_\mu\tilde{b}_{\alpha\beta}.\end{aligned} \tag{A.9}$$

Here the derivatives of $\tilde{H}$ and $\tilde{\kappa}$ w.r.t. $\tilde{a}_{\alpha\beta}$ and $\tilde{b}_{\alpha\beta}$, i.e. $\frac{\partial\tilde{H}}{\partial\tilde{a}_{\alpha\beta}}$, $\frac{\partial\tilde{H}}{\partial\tilde{b}_{\alpha\beta}}$, $\frac{\partial\tilde{\kappa}}{\partial\tilde{a}_{\alpha\beta}}$, and $\frac{\partial\tilde{\kappa}}{\partial\tilde{b}_{\alpha\beta}}$, are given in [31]. We thus obtain

$$\Delta_\mu\tilde{s} = \xi\ \left(-\tilde{b}^{\alpha\beta}\ \Delta_\mu\tilde{a}_{\alpha\beta} + \tilde{a}^{\alpha\beta}\ \Delta_\mu\tilde{b}_{\alpha\beta}\right) + \xi^2\ \left(-\tilde{\kappa}\ \tilde{a}^{\alpha\beta}\ \Delta\mu\tilde{a}_{\alpha\beta} + \tilde{\tilde{b}}^{\alpha\beta}\ \Delta_\mu\tilde{b}_{\alpha\beta}\right). \tag{A.10}$$

A.6. Linearization of $\tilde{\tau}^{\alpha\beta}$ and $\tilde{M}^{\alpha\beta}$ in the direction of $\Delta\mu$

We can derive the following linearizations

$$\begin{aligned}\Delta_\mu\tilde{\tau}^{\alpha\beta} &= \int_{-\frac{T}{2}}^{\frac{T}{2}} \left(1-\xi^2\kappa\right)\ \left[\Delta_\mu\tilde{s}\ \hat{\tilde{\tau}}^{\alpha\beta} + \tilde{s}\ \Delta_\mu\hat{\tilde{\tau}}^{\alpha\beta}\right]\ \mathrm{d}\xi,\\ \Delta_\mu\tilde{M}^{\alpha\beta} &= \int_{-\frac{T}{2}}^{\frac{T}{2}} \left(-\xi+\xi^2 H\right)\ \left[\Delta_\mu\tilde{s}\ \hat{\tilde{\tau}}^{\alpha\beta} + \tilde{s}\ \Delta_\mu\hat{\tilde{\tau}}^{\alpha\beta}\right]\ \mathrm{d}\xi,\end{aligned} \tag{A.11}$$

where $\hat{\tilde{\tau}}^{\alpha\beta}$ is given by Eq. (68). Its linearization yields

$$\Delta_\mu\hat{\tilde{\tau}}^{\alpha\beta} = \hat{G}_{\text{shear}}\left(\Delta_\mu\tilde{g}^{\alpha\beta} + 2\frac{\Delta_\mu J_{\text{el}}^\star}{J_{\text{el}}^{\star 3}}g^{\alpha\beta}\right), \tag{A.12}$$

A.7. Linearization of $\tilde{g}_{\alpha\beta}$ and $\tilde{g}^{\alpha\beta}$ in the direction $\Delta\mu$

The change of $\tilde{g}_{\alpha\beta}$ in the direction Δ_μ is given by

$$\Delta_\mu\tilde{g}_{\alpha\beta} = \tilde{g}_a\ \Delta_\mu\tilde{a}_{\alpha\beta} + \tilde{g}_b\ \Delta_\mu\tilde{b}_{\alpha\beta} + \tilde{a}_{\alpha\beta}\ \Delta_\mu\tilde{g}_a + \tilde{b}_{\alpha\beta}\ \Delta_\mu\tilde{g}_b \tag{A.13}$$

in which

$$\begin{aligned}\Delta_\mu\tilde{g}_a &= \xi^2\hat{\kappa}\ \tilde{a}^{\gamma\delta}\ \Delta_\mu\tilde{a}_{\gamma\delta} - \xi^2\ \breve{\tilde{b}}^{\gamma\delta}\ \Delta_\mu b_{\gamma\delta},\\ \Delta_\mu\tilde{g}_b &= -\xi^2\ \tilde{b}^{\gamma\delta}\ \Delta_\mu\tilde{a}_{\gamma\delta} - \xi^2\ \tilde{a}^{\gamma\delta}\ \Delta_\mu b_{\gamma\delta}.\end{aligned} \tag{A.14}$$

$\breve{\tilde{b}}^{\gamma\delta} = \tilde{\kappa}\ \tilde{b}_{\text{inv}}^{\gamma\delta} = 2\ \tilde{H}\ \tilde{a}^{\gamma\delta} - \tilde{b}^{\gamma\delta}$. Likewise, the change

$$\Delta_\mu\tilde{g}^{\alpha\beta} = \tilde{g}_a^{\alpha\beta\gamma\delta}\ \Delta_\mu\hat{a}_{\gamma\delta} + \tilde{g}_b^{\alpha\beta\gamma\delta}\ \Delta_\mu\tilde{b}_{\gamma\delta} \tag{A.15}$$

can be derived, with

$$\begin{aligned}\tilde{g}_a^{\alpha\beta\gamma\delta} &:= \tilde{s}^{-2}\left(\tilde{a}^{\alpha\beta}\ \tilde{\epsilon}_a^{\gamma\delta} + \tilde{b}^{\alpha\beta}\ \tilde{v}_a^{\gamma\delta}\right) + \tilde{g}^a\ \tilde{a}^{\alpha\beta\gamma\delta} + \tilde{g}^b\ \tilde{b}^{\alpha\beta\gamma\delta},\\ \tilde{g}_b^{\alpha\beta\gamma\delta} &:= \tilde{s}^{-2}\left(\tilde{a}^{\alpha\beta}\ \tilde{\epsilon}_b^{\gamma\delta} + \tilde{b}^{\alpha\beta}\ \tilde{v}_b^{\gamma\delta}\right) - \tilde{g}^b\ \tilde{a}^{\alpha\beta\gamma\delta},\end{aligned} \tag{A.16}$$

References

[1] S.A. Chester, L. Anand, A coupled theory of fluid permeation and large deformations for elastomeric materials, J. Mech. Phys. Solids 58 (11) (2010) 1879–1906.

[2] C.Y. Hui, Y.Y. Lin, F.C. Chuang, K.R. Shull, W.C. Lin, A contact mechanics method for characterizing the elastic properties and permeability of gels, J. Polym. Sci. Part B: Polym. Phys. 44 (2) (2006) 359–370.

[3] S. Cai, Y. Hu, X. Zhao, Z. Suo, Poroelasticity of a covalently crosslinked alginate hydrogel under compression, J. Appl. Phys. 108 (11) (2010) 113514.

[4] X. Zhao, N. Huebsch, D.J. Mooney, Z. Suo, Stress-relaxation behavior in gels with ionic and covalent crosslinks, J. Appl. Phys. 107 (2010) 063509.

[5] Q. Liu, G. Subhash, D.F. Moore, Loading velocity dependent permeability in agarose gel under compression, J. Mech. Behav. Biomed. Mater. 4 (7) (2011) 974–982.

[6] E.C. Achilleos, R.K. Prudhomme, K.N. Christodoulou, K.R. Gee, I.G. Kevrekidis, Dynamic deformation visualization in swelling of polymer gels, Chem. Eng. Sci. 55 (17) (2000) 3335–3340.

[7] J. Yoon, S. Cai, Z. Suo, R.C. Hayward, Poroelastic swelling kinetics of thin hydrogel layers: Comparison of theory and experiment, Soft Matter 6 (23) (2010) 6004–6012.

[8] J.Y. Sun, X. Zhao, W.R. Illeperuma, O. Chaudhuri, K.H. Oh, D.J. Mooney, J.J. Vlassak, Z. Suo, Highly stretchable and tough hydrogels, Nature 489 (7414) (2012) 133–136.

[9] H. Yuk, T. Zhang, S. Lin, G.A. Parada, X. Zhao, Tough bonding of hydrogels to diverse non-porous surfaces, Nature Mater. 15 (2) (2016) 190–196.

[10] B. Lu, H. Yuk, S. Lin, N. Jian, K. Qu, J. Xu, X. Zhao, Pure pedot: Pss hydrogels, Nature Commun. 10 (1) (2019) 1–10.

[11] M. Doi, Gel dynamics, J. Phys. Soc. Japan 78 (5) (2009) 052001-052001.

[12] T. Tanaka, D.J. Fillmore, Kinetics of swelling of gels, J. Chem. Phys. 70 (3) (1979) 1214–1218.

[13] W. Hong, X. Zhao, J. Zhou, Z. Suo, A theory of coupled diffusion and large deformation in polymeric gels, J. Mech. Phys. Solids 56 (5) (2008) 1779–1793.

[14] F.P. Duda, A.C. Souza, E. Fried, A theory for species migration in a finitely strained solid with application to polymer network swelling, J. Mech. Phys. Solids 58 (4) (2010) 515–529.

[15] S.A. Chester, L. Anand, A thermo-mechanically coupled theory for fluid permeation in elastomeric materials: Application to thermally responsive gels, J. Mech. Phys. Solids 59 (10) (2011) 1978–2006.

[16] M.A.C. Stuart, W.T. Huck, J. Genzer, M. Müller, C. Ober, M. Stamm, G.B. Sukhorukov, I. Szleifer, V.V. Tsukruk, M. Urban, F. Winnik, Emerging applications of stimuli-responsive polymer materials, Nature Mater. 9 (2) (2010) 101.

[17] L. Ionov, Soft microorigami: Self-folding polymer films, Soft Matter 7 (15) (2011) 6786–6791.

[18] J. Zhang, X. Zhao, Z. Suo, H. Jiang, A finite element method for transient analysis of concurrent large deformation and mass transport in gel, J. Appl. Phys. 105 (9) (2009) 093522.

[19] K.Y. Lee, M.C. Peters, K.W. Anderson, D.J. Mooney, Controlled growth factor release from synthetic extracellular matrices, Nature 408 (6815) (2000) 998–1000.

[20] W. Hong, Z. Liu, Z. Suo, Inhomogeneous swelling of a gel in equilibrium with a solvent and mechanical load, Int. J. Solids Struct. 46 (17) (2009) 3282–3289.

[21] W. Hong, X. Zhao, Z. Suo, Formation of creases on the surfaces of elastomers and gels, Appl. Phys. Lett. 95 (11) (2009) 111901.

[22] T. Tanaka, S.T. Sun, Y. Hirokawa, S. Katayama, J. Kucera, Y. Hirose, T. Amiya, Mechanical instability of gels at the phase transition, Nature 325 (6107) (1987) 796–798.

[23] V. Trujillo, J. Kim, R.C. Hayward, Creasing instability of surface-attached hydrogels, Soft Matter 4 (3) (2008) 564–569.

[24] I.J. Suarez, A. Fernandez-Nieves, M. Marquez, Swelling kinetics of poly (N-isopropylacrylamide) minigels, J. Phys. Chem. B 110 (51) (2006) 25729–25733.

[25] Y. Li, T. Tanaka, Kinetics of swelling and shrinking of gels, J. Chem. Phys. 92 (2) (1990) 1365–1371.

[26] T. Mora, A. Boudaoud, Buckling of swelling gels, Eur. Phys. J. E 20 (2) (2006) 119–124.

[27] V.M. Starov, S.A. Zhdanov, M.G. Velarde, Spreading of liquid drops over thick porous layers: Complete wetting case, Langmuir 18 (25) (2002) 9744–9750, [28].

[28] A. Nitti, J. Kiendl, A. Gizzi, A. Reali, M.D. de Tullio, A curvilinear isogeometric framework for the electromechanical activation of thin muscular tissues, Comp. Meth. Appl. Mech. Engrg. 382 (2021) 113877.

[29] E. Efrati, E. Sharon, R. Kupferman, Elastic theory of unconstrained non-Euclidean plates, J. Mech. Phys. Solids 57 (4) (2009) 762–775.

[30] N. Vu-Bac, T.X. Duong, T. Lahmer, X. Zhuang, R.A. Sauer, H.S. Park, T. Rabczuk, A NURBS-based inverse analysis for reconstruction of nonlinear deformations of thin shell structures, Comp. Meth. Appl. Mech. Engrg. 331 (2018) 427–455.

[31] N. Vu-Bac, T.X. Duong, T. Lahmer, P. Areias, R.A. Sauer, H.S. Park, T. Rabczuk, A NURBS-based inverse analysis of thermal expansion induced morphing of thin shells, Comput. Meth. Appl. Mech. Engrg. 350 (2019) 480–510.

[32] C.L. Thanh, L.V. Tran, T. Vu-Huu, M. Abdel-Wahab, The size-dependent thermal bending and buckling analyses of composite laminate microplate based on new modified couple stress theory and isogeometric analysis, Comput. Meth. Appl. Mech. Engrg. 350 (2019) 337–361.
[33] T. Cuong-Le, K.D. Nguyen, N. Nguyen-Trong, S. Khatir, H. Nguyen-Xuan, M. Abdel-Wahab, A three-dimensional solution for free vibration and buckling of annular plate, conical, cylinder and cylindrical shell of FG porous-cellular materials using IGA, Compos. Struct. 259 (2021) 113216.
[34] H.X. Nguyen, T.N. Nguyen, M. Abdel-Wahab, S.P. Bordas, H. Nguyen-Xuan, T.P. Vo, A refined quasi-3D isogeometric analysis for functionally graded microplates based on the modified couple stress theory, Comput. Meth. Appl. Mech. Engrg. 313 (2017) 904–940.
[35] P. Phung-Van, L.V. Tran, A.J.M. Ferreira, H. Nguyen-Xuan, M.J.N.D. Abdel-Wahab, Nonlinear transient isogeometric analysis of smart piezoelectric functionally graded material plates based on generalized shear deformation theory under thermo-electro-mechanical loads, Nonlinear Dynam. 87 (2) (2017) 879–894.
[36] P. Phung-Van, C.H. Thai, H. Nguyen-Xuan, M.A. Wahab, Porosity-dependent nonlinear transient responses of functionally graded nanoplates using isogeometric analysis, Compos. B. Eng. 164 (2019) 215–225.
[37] M. Pezzulla, S.A. Shillig, P. Nardinocchi, D.P. Holmes, Morphing of geometric composites via residual swelling, Soft Matter 11 (29) (2015) 5812–5820.
[38] M. Pezzulla, G.P. Smith, P. Nardinocchi, D.P. Holmes, Geometry and mechanics of thin growing bilayers, Soft Matter 12 (19) (2016) 4435–4442.
[39] M. Pezzulla, N. Stoop, M.P. Steranka, A.J. Bade, D.P. Holmes, Curvature-induced instabilities of shells, Phys. Rev. Lett. 120 (4) (2018) 048002.
[40] P.J. Flory, Thermodynamics of high polymer solutions, J. Chem. Phys. 10 (1) (1942) 51–61.
[41] M.L. Huggins, Some properties of solutions of long-chain compounds, J. Phys. Chem. 46 (1) (1942) 151–158.
[42] C. Zimmermann, D. Toshniwal, C.M. Landis, T.J. Hughes, K.K. Mandadapu, R.A. Sauer, An isogeometric finite element formulation for phase transitions on deforming surfaces, Comput. Meth. Appl. Mech. Engrg. 35 (2019) 441–477.
[43] P.M. Naghdi, The theory of shells and plates, in: Flugge's Handbuch Der Physik, Vol. VI a/C, Truesdell, 1972.
[44] D.J. Steigmann, On the relationship between the cosserat and Kirchhoff–Love theories of elastic shells, Math. Mech. Solids 4 (3) (1999) 275–288.
[45] R.A. Sauer, T.X. Duong, On the theoretical foundations of thin solid and liquid shells, Math. Mech. Solids 22 (3) (2015) 343–371.
[46] R.A. Sauer, R. Ghaffari, A. Gupta, The multiplicative deformation split for shells with application to growth, chemical swelling, thermoelasticity, viscoelasticity and elastoplasticity, Int. J. Solids Struct. 174 (2019) 53–68.
[47] V.A. Lubarda, Constitutive theories based on the multiplicative decomposition of deformation gradient: Thermoelasticity, elastoplasticity, and biomechanics, Appl. Mech. Rev. 57 (2) (2004) 95–108.
[48] S.A. Chester, C.V. Di Leo, L. Anand, A finite element implementation of a coupled diffusion-deformation theory for elastomeric gels, Int. J. Solids Struct. 52 (2015) 1–18.
[49] P.J. Flory, J. Rehner Jr., Statistical mechanics of cross-linked polymer networks II, Swelling. J. Chem. Phys. 11 (1943) 521–526.
[50] T.X. Duong, F. Roohbakhshan, R.A. Sauer, A new rotation-free isogeometric thin shell formulation and a corresponding continuity constraint for patch boundaries, Comput. Meth. Appl. Mech. Engrg. 316 (2017) 43–83.
[51] M.F. Beatty, Topics in finite elasticity: Hyperelasticity of rubber, elastomers, and biological tissues—with examples, Appl. Mech. Rev. 40 (12) (1987) 1699–1734.
[52] A. Lucantonio, P. Nardinocchi, M. Pezzulla, L. Teresi, Multiphysics of bio-hybrid systems: Shape control and electro-induced motion, Smart Mater. Struct. 23 (4) (2014) 045043.
[53] R.T. Haftka, Z. Gürdal, Elements of Structural Optimization, Springer Science & Business Media, 2012.
[54] S.S. Nanthakumar, T. Lahmer, X. Zhuang, G. Zi, T. Rabczuk, Detection of material interfaces using a regularized level set method in piezoelectric structures, Inverse Probl. Sci. Eng. 24 (1) (2016) 153–176.
[55] T.J.R. Hughes, J.A. Cottrell, Y. Bazilevs, Isogeometric analysis: CAD, finite elements, NURBS, exact geometry and mesh refinement, Comput. Meth. Appl. Mech. Engrg. 194 (39–41) (2005) 4135–4195.
[56] R.A. Sauer, T.X. Duong, K.K. Mandadapu, D.J. Steigmann, A stabilized finite element formulation for liquid shells and its application to lipid bilayers, J. Comput. Phys. 330 (2017) 436–466.